LAWRENCE
LIVERMORE
NATIONAL
LABORATORY

LLNL-JRNL-859079

Transmission Electron Microscopy of the Rapid Solidification Microstructure Evolution and Solidification Interface Velocity Determination in Hypereutectic Al-20at.%Cu After Laser Melting

Y. Liu, K. Zweiacker, C. Liu, J. T. McKeown, J. Wiezorek

January 11, 2024

Acta Materialia

Disclaimer

LLNL-JRNL-859079

Transmission electron microscopy of the rapid solidification microstructure evolution and solidification interface velocity determination in hypereutectic Al-20at.%Cu after laser melting

Y. Liu,[1] K. Zweiacker,[1,3] C. Liu,[1] J.T. McKeown,[2] J.M.K. Wiezorek[1,*]

[1] Department of Mechanical Engineering and Materials Science, University of Pittsburgh, 636 Benedum Hall, 3700 O'Hara Street, Pittsburgh, PA 15261, USA
[2] Materials Science Division, Physical and Life Sciences Directorate, Lawrence Livermore National Laboratory, 7000 East Avenue, Livermore, CA 94551, USA
[3] Now at Hitachi Energy, Zürich, CH, USA

Abstract

The evolution of rapid solidification (RS) microstructure and solidification interface velocity has been studied experimentally by in-situ transmission electron microscopy and postmortem characterization for hypereutectic Al-20at.%Cu (37 wt.%Cu) after laser melting. Four morphologically distinct regions formed via growth modes changing from θ-Al_2Cu phase dendrites to eutectic cell growth, possibly α-Al dendrite growth (α-cell), banded growth, and α-Al plane front growth. Tendency for faceting and low capacity for solute trapping limited the θ-phase dendrite growth to solidification interface velocity $v < 0.07$ m/s. Consequently, formation of pro-eutectic micro-constituent was suppressed, and RS microstructure formation was dominated by eutectic, α-cell, and banded morphology grains for the Al-20at.%Cu alloy. Eutectic growth operated for interface velocity of 0.1 m/$s \leq v < 0.3$ m/s, with a transition from regular lamellar, 2-λ and 1-λ mode to a dense irregular morphology dominated by α-phase at $v = 0.3$ m/s. Interface temperature calculations indicated feasibility of α-cell growth mode for 0.3 m/$s \leq v <$ 0.7 m/s. Banded growth occurred for 0.7 m/$s \leq v < 1.3$ m/s. Plane front α-phase growth was evident for interface velocities $v \geq 1.3$ m/s. Previous work on rapid solidification microstructure development in hypereutectic Al-Cu alloys reported a regime of α-cell growth subsequently to eutectic and prior to transition to banded growth for Al-19at.%Cu (36 wt.%Cu), while for Al-22at.%Cu (40 wt.%Cu) eutectic growth transitioned directly to α-plane front growth without emergence of a banded regime. Based on the current study the disappearance of the banded growth regime occurs for a composition larger than 20at.%Cu.

*Corresponding author.
Email address: wiezorek@pitt.edu (J.M.K. Wiezorek)

1. Introduction

Rapid solidification (RS) is responsible for the microstructure development during liquid-solid processing of alloys with high-energy-density laser and electron beam methods [1–8]. A scientifically sound understanding of alloy and processing method specific aspects of RS is therefore desirable to take advantage of this first opportunity for controlling microstructure and associated properties. Large cooling rates, typically in the range of 103 K/s to 107 K/s, have been reported for RS of metals and alloys [9]. These give rise to large maximal interfacial supercooling on the order of 101 K to 102 K and solidification rates up to102 m/s [9–11]. Compared with more conventional solidification processes, such as casting with cooling rates ranging from10 2 K/s for furnace cooling to 102 K/s for continuous strip casting processes of Al alloys, RS is associated with extreme conditions [9,12]. During RS after laser or electron beam melting, alloy microstructures are formed behind an accelerating solidification interface that has been driven far away from equilibrium and exhibit non-equilibrium characteristics, such as excessive solute trapping, formation of metastable and unexpected phases, and refinements of the relevant microstructural length scales, including grain size, secondary constituents, and phases [3,5,8,9]. For increasing solidification interface velocity, v, stability analysis predicts a sequence of morphological transitions for the growth interface, i.e., from an initially plane front to cellular, followed by cellular to dendritic, then from dendritic to cellular, and finally again to plane front growth [4,13, 14]. These velocity dependent growth mode changes engender alloy dependent changes in the RS microstructure, e.g., the level of solute trapping, and the type, scale, and morphology of the constituent phases [6,9,15]. Theoretical models of RS, such as the continuous growth model (CGM) and local non-equilibrium model (LNM), describe the non-equilibrium conditions at the solidification interface via interface response functions that depend on the solidification interface velocity, v, and composition, X, such as the non-equilibrium interface partition coefficient, k(v,X), and the interfacial temperature, T_i(v,X) [16,17]. They have been used successfully to describe the conditions at the accelerating solidification interface during RS for dilute alloys and attempts have been made to extend modeling to concentrated alloys [18]. Many technologically relevant alloys are concentrated multicomponent systems with performance properties depending on their unique and usually multiphase microstructures, e.g., some commercial precipitation strengthened Al- and Ni-alloys and the emerging class of multiple-principle-element alloys, also referred to as high-entropy alloys. To support further development of accurate theoretical models and to enable reliable and predictive computer simulations of RS of concentrated multicomponent alloys during electron- and laser-beam processing, which includes several promising additive manufacturing technologies, additional experimental research is required [18–22].

The unique nanoscale spatiotemporal resolution afforded by the dynamic transmission electron microscope (DTEM), inclusive of operation in movie-mode, i.e., movie-mode DTEM (MM-DTEM) experiments, and the ability to use pulsed laser irradiation to melt local regions of thin films of metals and alloys has facilitated direct observations of the migrating RS interface by in-situ TEM imaging [6,8,15,23]. For example, determination of the evolution of the velocity of the accelerating solidification interface during RS after laser melting of Al and several

concentrated Al alloys has been enabled by MM-DTEM with temporal resolution equivalent to in-situ imaging at a nominal frame rate of 4×105 frames per second (fps) [7,8,15,23]. The thin film specimens used in MM-DTEM experiments have thicknesses in the range of 50 nm to 200 nm to maintain electron transparency [24,25]. The laser pulse creates a melt pool that extends through the entire thickness of the metal or alloy layer of the thin film specimen, thickness ≤ 0.2 µm, with lateral dimensions that are about three orders of magnitude larger, diameters in the range of 50 µm to ≈100 µm (Fig. 1) [24,25]. The liquid melt is laterally confined by the solid metal or alloy of the thin film and its other two surfaces bounded by an amorphous Si3N4 membrane and vacuum or an amorphous oxide cap-layer (Fig. 1) [24,25]. The highly anisotropic geometry ensures dominance of the directional thermal transport during cooling of the superheated melt by conduction radially outward through the interface between the melt and the adjacent metal or alloy solid surrounding it [24]. Hence, crystal growth is epitaxially seeded by the grains of the metal or alloy solid at the solid-liquid boundary defining the melt pool prior to solidification and occurs by directional RS [24, 25]. The nanoscale thickness of the liquid melt layer results in scenarios that approximate two-dimensional growth for solidification conditions associated with dendrite tip curvature exceeding the thin film sample thickness. For RS conditions where nanoscale dimensions result in more significant dendrite tip effects occurring along the thin direction of the electron transparent specimens associated effects on solidification conditions must be accounted for. Use of nanocrystalline grain size metals or alloys ensures that homogeneous liquid compositions can be accomplished in the melt prior to the start of RS. Also, the scale of interface section of seed crystals with the liquid, ≤ 200 nm, is very small relative to the total circumferential length of the initial solid-liquid interface of the melt pool, > 200 µm. Therefore, at length scales of ≈1 µm to good approximation self-similar conditions exist along the solid-liquid interface prior to the onset of RS. If that is not the case, e.g., if the scale of grains of the pro-eutectic phase and the regions associated with eutectic constituent in a hypoeutectic alloy approaches a significant fraction, e. g., say 10%, of the circumferential length of the melt pool boundary, locally the conditions will be different at the beginning of the RS processes, since compositions in liquid and solid seed crystal differ for the two different microstructural constituents of the solid alloy. This will manifest itself during RS microstructure formation by rendering it more heterogeneous. The geometric constraints imposed by the nanocrystalline thin film use and melting by an irradiation pulse from a stationary laser in vacuum on the directional RS crystal growth processes provide for quite well-defined thermal and constitutional conditions during MM-DTEM in-situ RS experiments. Many effects that make it difficult to compare quantitatively the results of computer modeling with experimental observations of RS microstructure evolved after scanned laser melting or from powders in concentrated alloys are strongly reduced or avoided in MM-DTEM RS experiments. For instance, effects from complex fluid dynamics (Marangoni flow), convective mixing in the resulting three-dimensional melt pools, which have comparable depth and width dimensions usually on the scale of 101 to 102 µm, the complex three-dimensional changes of the maximal thermal gradients across different sections of the multi-dimensionally curved solidification interface created by the scanned laser, as well as entrainment of gas do not play important roles during MM-DTEM RS experiments.

Furthermore, direct observation of the advancing solidification interface via MM-DTEM imaging after laser melting permits determination not only of average values but also the local values for the solidification interface velocity [8,15,24]. In combination with site-specific postmortem studies of the microstructure the knowledge of the magnitude of the solidification interface velocity at these localities permits quantitative correlation with the respective growth modes responsible for the details of the non-equilibrium microstructure. In comparison with scanned laser surface melting of bulk alloy or powders the MM-DTEM experiments offer characteristics that are advantageous for direct comparison with theory predictions and to support computer modeling of RS microstructure evolution, for instance by providing mechanistic details of the non-equilibrium phase transformations and crystal defect genesis [6,8, 20,24,26].

The Al-rich side and compositions up to Al_2Cu (33.6 atomic percent, at.%, Cu) of the binary Al-Cu system represents a classic eutectic system with α-Al and θ-Al_2Cu as terminal phases, a eutectic point at 821K≈548 ◦C and ≈17 atomic percent (at.%) Cu [27]. Since reliable thermophysical data are available, concentrated Al-Cu alloys in this composition range have served as a useful model system for detailed studies of RS microstructure evolution after laser melting [3,4,8,15,25, 28–31]. Under conditions deviating only moderately from equilibrium the solidification of hypoeutectic Al-Cu alloys involves as a primary product the pro-eutectic α-Al and as a secondary product the eutectic constituent, comprised of α-Al and θ-Al_2Cu and with lamellar morphology [27]. In hypereutectic compositions the primary solidification product would change to θ-Al_2Cu and eutectic as a secondary product would remain [27]. Experimental studies of RS in hypoeutectic Al-Cu alloys, compositions, C0, 4 at.% Cu ≤ C0 ≤ 14 at.% Cu, reported solidification microstructures that characteristically exhibited four morphologically distinct zones, namely, a heat-affected zone (HAZ), a transition zone, a columnar grain zone and a zone of banded morphology grains [6,8,15,29–31]. Directional RS crystal growth is seeded epitaxially by the solid grains formed in the HAZ, slightly supersaturated α-Al grains and intergranular regions containing θ-Al_2Cu, located at the boundary with the melt pool [6,8,15,30,31]. In the transition zone, pro-eutectic α-Al solid solution grains formed as the primary product behind an interface transitioning from planar to cellular and then to dendritic growth as the initially stationary solidification interface accelerated rapidly at the onset of directional RS [8]. This initial stage represents cellular α-Al RS growth and invokes significant Cu solute trapping prior to a morphological change in the microstructure during dendritic growth, which occurs for critical values of the solidification interface velocity that decrease as the Cu fraction increases for the hypoeutectic alloys [6,8,15,29–31]. This transition from dendritic to eventually cellular mode defines the onset of the columnar grain zone in the RS microstructure of hypoeutectic Al-Cu alloys, also referred to as α-cells, and forms by a non-equilibrium mode of dendritic or cellular growth of supersaturated α-Al and nanoscale Al_2Cu as a secondary interdendritic or intercellular solidification product [8,29–31]. As the solidification interface velocity increases during this α-cell growth the scale and morphology of the secondary product change and at the highest migration rates in this RS growth regime the metastable θ‘-Al_2Cu phase replaces the thermodynamically stable θ-Al_2Cu phase [8,15, 29–31]. Finally, the zone of banded morphology grains begins to form when the solidification interface velocity, v, reaches another critical value,

namely, $v = v_a$, the velocity of absolute stability [3,4,6,8,14,15, 25,29–31]. At this critical solidification interface velocity, v_a, the magnitude of which decreases with increasing Cu content for hypoeutectic Al-Cu, a final growth mode transition from modified dendrite growth of α-cells to α-Al phase plane front growth leads to formation of the first single-phase bands of the banded morphology grains [6,8,15, 29–31]. In contrast, for the eutectic Al-17at.%Cu alloy the RS microstructure evolution involves a single growth mode transition as the solidification interface velocity increases from initially eutectic growth at lower velocities to α-phase plane front growth when the accelerating solidification interface reaches the critical velocity of $v = v_a$ [28,31]. As the solidification interface accelerates during eutectic growth the lamellar spacing of the regular eutectic refines and changes to irregular morphologies prior to the transition to α-phase plane front growth and banded morphology grain formation [28]. Unlike for the primary RS product of α-Al solid solution phase in hypoeutectic Al-Cu alloys, which is expected to establish an atomically rough solid-liquid growth interface typical of metals, for RS of hypereutectic Al-Cu alloys the primary product of θ-Al_2Cu phase is expected to exhibit tendencies for facetted solidification interface behaviors [31]. θ-Al_2Cu is an intermetallic phase with a compositionally layered and chemically ordered tetragonal crystal structure, a relatively narrow composition range, 32.1 at.% Cu to 33.6 at.% Cu, a liquidus line that differs considerably from linear and a solidus line with a very steep slope [27]. These characteristics imply a low capacity for Al solute trapping, a very steep T0-line for partitionless solidification, and significant effects of solute drag on the driving force for growth of θ-Al_2Cu [3,4,31]. A limited range for solidification interface velocities and an associated large rate of interfacial undercooling for θ-Al_2Cu growth, i.e., via cellular and dendritic modes, is therefore expected during RS after laser melting of hypereutectic Al-Cu alloys. This is consistent with previously reported predictions of a reduced θ-phase dendrite growth regime and conversely expanded eutectic growth regime, which were based on numerical calculations for RS growth modes in a hypereutectic Al-22at.%Cu alloy [31]. Effects of the reasonably expected differences between the RS behaviors of the solid solution phase of α-Al and the intermetallic phase of θ-Al_2Cu can also be inferred from the characteristic morphological changes revealed in the α-cell growth regime of hypoeutectic alloys [6,8,15,29–31].

In contrast to the hypoeutectic Al-Cu alloys there is a distinct lack of experimental studies of RS microstructure evolution in hypereutectic Al- Cu alloys [29,30]. Hence, here we performed in-situ MM-DTEM experiments to study the solidification microstructure formation after laser irradiation induced melting in Al-Cu alloy of hypereutectic composition. Complementary postmortem TEM/STEM studies of the resulting solidification microstructure facilitated locally resolved composition and structural analyses. The current paper presents experimental measurements of solidification interface velocity and the genesis of the associated microstructure during the solid-liquid-solid transformation sequence after laser melting for a hypereutectic binary alloy Al-20 at.% Cu (Al-20Cu for short). Nanoscale resolved measurements of the morphology, scale, phase constitution and composition of distinct regions of the RS microstructures of Al-20Cu are related to the local solidification interface velocity. Effects of the crystal growth characteristics of the chemically ordered Al_2Cu intermetallic phase and the chemically disordered Al solid solution phase on the solidification interface velocity dependent

selection of the growth modes are discussed. The results obtained for the hypereutectic Al-20Cu alloy are compared to prior reports for experiments on concentrated Al-Cu alloys [6,8,15,25,28–31].

2. Experimental procedures

Thin films of hypereutectic Al-Cu alloy with a nominal composition of 20 atomic percent (at.%) Cu and a nominal thickness of 160 nm were prepared by double electron beam evaporation (Pascal Technologies Dual E-Beam Deposition System). The 50 nm thick amorphous Si3N4 membranes of windowed Si-TEM-grids (Ted Pella Inc.) with 500 µm x 500 µm square windows were used as substrates for the Al-Cu alloy film depositions (e.g., Fig. 1) [6,8,15]. Electron beam deposition was performed in a high vacuum (base pressure $< 5 \times 10^{-8}$ torr = 6.7 x 10^{-6} Pa) at deposition rates of 2.0 - 2.5 nm/s using high-purity elemental Al and Cu targets, with the substrate held at 298 K. Surface profilometer measurements were performed to confirm film thickness.

The in-situ transmission electron microscopy experimentation has been performed by movie-mode DTEM (MM-DTEM) at 200 kV [23]. Individual melt pools were generated in the thin film in regions of the electron transparent window of the TEM samples by a single laser irradiation pulse of approximately 15 ns duration with an Nd: YAG laser, 1064 nm wavelength and Gaussian beam profile. Due to the pulsed laser irradiating the thin film samples at 45˚-angle of incidence the resulting melt pools developed an elliptical shape with a major axis diameter about 40% larger than the minor axis diameter [24]. For each windowed TEM grid sample up to five spatially separated melt pools were generated by pulsed laser irradiation. The individual 256×256 pixel images generated by the MM-DTEM experiments have been recorded by a 2kx2k CCD camera with single electron detection capability [23]. As detailed in prior works [24], a single MM-DTEM in-situ imaging series consisted of nine multi-beam bright-field TEM images acquired with an exposure time of 50 ns per image and delay time interval of 2.5 µs between subsequent images. Therefore, each MM-DTEM in-situ experiment recorded dynamics of the laser pulse irradiation stimulated response of the alloy microstructure for a duration totaling 20.45 µs =20 µs. For each of the MM-DTEM experiments an image was acquired after the completion of the microstructural transformation to record the final state, i.e., the ‘after-image’. The MM-DTEM image series were acquired in low-magnification mode of the TEM instrument to attain large fields of view that can facilitate capture of the entire elliptically shaped melt pool during the sequence of solid-liquid-solid transformation of RS after pulsed laser irradiation. Significant differences in the electron scattering potentials for the solid crystalline and liquid alloy enabled quantification of the evolution of the liquid region as a function of time after the pulsed laser irradiation and thus the solidification rate and its changes. More detail on the MM-DTEM experimental procedures, quantitative image analysis, data processing and numerical analysis used for the determination of the solidification interface velocity evolution have been described in previous publications [24].

Postmortem microstructural characterization and analysis by transmission electron microscopy (TEM) and scanning TEM (STEM) utilized an aberration corrected Titan3 G2 60–300

S/TEM (FEI/ThermoFisher Scientific) operated at 300 kV and a Tecnai G2 F20 UT (FEI/ ThermoFisher Scientific) and a JEM 2100F S/TEM (JEOL) operated at 200 kV. The elemental composition has been determined by STEM energy-dispersive X-ray spectroscopy (EDXS) performed with a 0.18 nm diameter electron probe and step size equal to the probe diameter using the Titan3 G2 60–300 S/TEM and Chemi-STEM (Thermo Fisher Scientific). Individual pixels in composition maps have spatial areal dimensions of $(1.6\ nm)^2$ and display elemental compositions as the averaged signals of (9×9)-arrays from the original STEM EDXS scan data sets, resulting in elemental composition maps with an effective spatial resolution of about 2 nm laterally. To quantify composition from EDXS measurements, the k-factors for Cu and Al have been determined experimentally using the stoichiometric composition θ-Al_2Cu established in annealed Al-Cu alloy films. In addition to selected area electron diffraction pattern acquisition for phase identification, crystallographic analyses of the alloy films were performed by precession electron diffraction-assisted automated crystal orientation mapping (PED-ACOM) in the TEM using an ASTAR system with Topspin acquisition software (NanoMEGAS) in conjunction with the JEM 2100F S/TEM (JEOL) [32]. The PED data acquisition used a 0.7˚ precession angle, 100 Hz precession frequency, and recorded 50 PED patterns per second for a relatively large nominal electron beam probe size of 14 nm with a step-size of 14 nm for large fields of view of the RS microstructure. Between 200,000 to 300,000 PED patterns were collected within about 1.5 h to 3 h for the phase and orientation maps. The orientation and phase maps for the hypereutectic Al-20Cu alloy were generated by indexing of the PED patterns via a vendor-proprietary (NanoMEGAS) computer-automated process that matched them to calculated reciprocal lattice templates of three phases: FCC α-Al, thermodynamically stable tetragonal θ-Al_2Cu and metastable tetragonal θ'-Al_2Cu. The orientation resolution is limited to 1˚by the reciprocal lattice templates used [32]. To identify low-certainty indexed voxels in the PED-ACOM data sets, which typically were associated with locations of grain boundaries and overlap of multiple phases through the thin film specimen thickness, the certainty index (CI) threshold values of $CI < 10$ were used in the Topspin software. Such low-certainty or poorly indexed voxels were reassigned the phase of neighboring voxel with the higher CI value for $CI \geq 10$. This approach ensured that only high-quality phase indexed data were used in the ACOM phase maps and associated analysis, leading to more reliable and accurate results.

3. Results and discussion

3.1. As-deposited state of the Al-20Cu alloy

The as-deposited thin films of Al-20Cu alloy exhibited a nanocrystalline microstructure comprised of morphologically equiaxed grains of α-Al and θ-Al_2Cu (Fig. 2). The bright and dark contrast regions in the STEM image indicate the presence of two types of compositionally different phases (Fig. 2a). This has been confirmed by the selected area diffraction pattern (SADP) analysis which detected the presence of α-Al and θ-Al_2Cu phase (Fig. 2.c). From the annular dark field (ADF) STEM image shown in Fig. 2a grain sizes in the range of 25 - 40 nm have been determined. Therefore, there is an inevitable overlap between individual grains through the film thickness in TEM/STEM images and for the analytically probed volumes in associated EDXS composition

analysis. The EDXS Cu-composition map of Fig. 2b and the example Cu content measurements summarized in tabulated form in Fig. 2d show that the average alloy film composition is 20.2 at.% Cu, and that the dark contrast grains and bright contrast grains in the image of Fig. 2a have on average composition of about 3.7 at.% Cu and 33.7 at.% Cu, respectively. The overlap with the θ-Al_2Cu phase grains, which are significantly enriched in Cu relative to the alloy composition (Fig. 2d), likely resulted in overestimates of the actual Cu content of the α-Al grains (Fig. 2b, d). The minimum Cu content of the α-Al grains has been determined as 2.8 at.% Cu (Fig. 2). It appears reasonable to conclude that the as-deposited Al-20Cu alloy was comprised of nanoscale grains of α-Al that are slightly supersaturated in Cu relative to the equilibrium maximum solubility of 2.5 at.% Cu and nanoscale grains of θ-Al_2Cu with equilibrium composition. This is consistent with the microstructural characteristics reported previously for Al-Cu thin films of hypoeutectic compositions prepared under equivalent conditions [6,8].

3.2. Movie-mode dynamic TEM in-situ rapid solidification experiments

The solid-liquid interface velocity evolution after pulsed laser irradiation induced melting has been determined for the hypereutectic Al- 20Cu alloy by direct observation using MM-DTEM experiments (Fig. 3) [23]. Seven low magnification multi-beam bright field MM-DTEM image sequences, each of 20 μs duration and comprised of nine 50 ns exposure images with 2.5μs frame-to-frame time intervals, are shown in Fig. 3a together with a tenth image taken nominally at infinite time after pulsed laser irradiation, the 'after-image'. Applying the same pulsed laser parameters, each image sequence has been acquired in a separate in-situ MM-DTEM experiment performed for seven different delay times after application of the laser melting pulse of 0 μs, 20 μs, 40 μs, 60 μs, 80 μs, 100 μs, and 120 μs, respectively (Fig. 3a). The total duration of the in-situ observations of nominally 140 μs enabled capture of the entire sequence of the solid-liquid-solid phase transformation after PL irradiation. The 'after images' consistently revealed three regions with distinct contrast for the RS microstructure of the hypoeutectic Al-20Cu alloy (e.g., see labels A, B and C in 'after-images' in Fig. 3a). Namely, an outer region in dark gray contrast (Zone A), adjacent to a morphologically similar cellular region exhibiting lighter gray contrast (Zone B) and a central region with more complex contrast features (Zone C) (Fig. 3a). The maximum outer perimeters of the dark gray regions (Zone A), e.g., marked as the red dashed ellipses in Fig 3a, represent the fully melted liquid alloy area established through the entire thickness of the alloy layer of the thin film by the laser pulse irradiation [6]. For the light gray contrast regions of Zone B of the RS microstructure the outer perimeter is marked by cyan colored dashed lines and a yellow dashed line delineates it from the central region of Zone C (Fig. 3a, see online version for color).

In the first MM-DTEM image sequence acquired with a delay time of 0μs after application of the laser pulse, the whole field of view has been melted (first row of images in Fig 3a)). Unfortunately, the melt pool dimension initially established by the laser irradiation pulse marginally exceeds the field of view of the MM-DTEM image sequence in the second image. The geometry of the approximately 45˚angle of incidence of the laser irradiation to the alloy film generates an elliptical shape melt pool with the major diameter equal to about 140% of the minor

diameter [24]. Knowledge of the geometry of the laser illumination and the resulting elliptical melt pool permits the determination of melt pool areas even for the MM-DTEM images that do not capture the liquid area in its entirety. The maximum dimensions inclusive of the major and minor diameters of the full through-film thickness melt pool areas are marked in the 'after-images' by red color dashed line elliptical shapes (right-hand-side, Fig. 3a, see online for color). These regions, marked as A, B and C in Fig. 3a, represent the area of the alloy microstructure established by directional crystal growth during RS and permit the identification of the directions of the major and minor axes of the initial melt pool caused by the laser pulse irradiation for each MM-DTEM image series. The rate of the changes in liquid area and thus the solidification interface velocity averaged along the solid-liquid interface perimeter have been determined by tracking the changes in the dimensions of the liquid regions along the directions of minor and major radii of the initially elliptically shaped melt pool and are summarized graphically in Fig. 3b [8,24]. The sequences of MM-DTEM images for the regimes marked as *Incubation, Stage I, Stage II*, and *Stage III* in Fig. 3a correspond to the respective solidification interface velocity regimes referenced in Fig. 3b for which distinctly different accelerations have been observed. In analogy to MM-DTEM in-situ RS microstructure evolution studies performed for hypoeutectic Al-alloys, these different interface acceleration regimes are expected to be associated with different crystal growth modes that establish morphologically different regions in the RS microstructure of the hypereutectic Al-20Cu alloy, i.e., a heat affected zone (HAZ), and Zone A, Zone B and Zone C (Fig. 3) [6,8, 24].

During the first 13 frames of the MM-DTEM image series collated in Fig. 3a, 0 µs to 27.5 µs after the laser pulse irradiation, the area of the liquid region did not monotonically decrease. This initial period after pulsed laser irradiation is associated with formation of the HAZ microstructure and has been labeled as *Incubation* in Fig. 3b. Notably, in the fourth and subsequent images of the first image sequence in Fig. 3a (marked 0 µs) a lighter gray contrast region becomes visible at the perimeter of the field of view (e.g., see near the locations marked by yellow arrows, Fig. 3a). This lighter gray region emerging in the MM-DTEM images corresponds to the coarsened crystalline grains formed in the HAZ [15]. Details of the HAZ are shown in postmortem acquired TEM/STEM images of Fig. 4, Fig. 5, and Fig. 6a. The HAZ microstructure is the result of re-solidification of a partially melted region that surrounds the central region where the alloy is melted through the entire thickness of the thin film [15,24]. The presence of the partially melted regions surrounding the superheated fully melted central melt pool is a consequence of the Gaussian temperature profile created by the laser pulse [15,24]. Here nanocrystalline α-Al and θ-Al_2Cu grains of the as-deposited thin film microstructure coexist for a limited time with liquid alloy. During the directional cooling after the pulsed laser application the area of the partially melted region shrinks, and retained solid grains grow larger during their solidification as the temperature sweeps through the phase specific solidification range. Subsequently, as temperatures drop below the eutectic isotherm coupled growth establishes eutectic microconstituent from liquid retained. The behavior of the hypereutectic alloy during the *Incubation* period is therefore expected to be analogous to the scenario described previously for the HAZ microstructure formation during the re-solidification after pulsed laser melting in

hypoeutectic Al-Cu alloys with the proviso that the primary pro-eutectic product is changed from α-Al phase to θ-Al_2Cu phase [15]. Due to the low magnification of MM-DTEM images acquired during the *incubation* period, which lasted for about 27–28 μs, only the cumulative effects of the crystal growth process responsible for forming the HAZ can be discerned (Fig. 3a). The width of the light gray contrast regions initially emerging at locations outside of the maximum scale of the directional crystal growth facilitated RS microstructure (e.g., red color (online) dashed line markers shown for some select images in first MM-DTEM imaging series, 0μs delay, Fig. 3a) increases for the time interval of about 10 μs to 27.5 μs after laser pulse application, i.e., for the 4th to the 13th image frame in the first and second MM-DTEM image series shown in Fig. 3a. Towards the end of the *Incubation* period, e.g., the first three frames in the MM-DTEM image sequence acquired after 20 μs delay (Fig. 3a), a stagnant liquid-solid interface with planar morphology at the scale of the spatial resolution of the MM-DTEM images is established through the entire thickness of the thin film [6–8,15]. Once the thermal profiles across this liquid-solid interface favor solid growth into the superheated through-thickness alloy melt directional RS crystal growth processes ensue to form the RS microstructure with its *Zone A, Zone B* and *Zone C* (marked as Stage I in Fig. 3a).

For the MM-DTEM image sequence in Fig. 3a the maximum size of the elliptical melt pool prior to the onset of directional RS at the end of the *Incubation* period has been determined from the 14th image, i.e., the fifth frame of the second row for a nominal delay of 30 μs, with radii of 37 μm and 33 μm along the semi-major and semi-minor axes, respectively. Considering that the RS microstructure of the hypereutectic Al- 20Cu alloy developed its three morphologically distinct regions during directional crystal growth that lasted for a duration of about 100 μs, an average solidification interface velocity of about 0.34 m/s to 0.37 m/s can be estimated (Fig. 3b). The upper and lower limits for the solidification interface velocity plotted in Fig. 3b for *Stage I* (27.5 μs < t ≤ 70 μs) and *Stage II* (70 μs < t ≤ 107.5 μs) represent the velocity along the directions of the major and minor radii of the initially elliptical shape melt pool (Fig. 3b). The solidification interface velocity data shown for *Stage III* in Fig. 2b (107.5 μs < t ≤ 127.5 μs) has been obtained by tracking the area reduction of the liquid region observed in the last nine MM-DTEM images prior to completion of solidification at 127.5 μs to 130 μs. During most of the RS in *Stage I*, 27.5 μs < t ≤ 70 μs, the solidification interface accelerated with an average constant acceleration a_I = 4250 ms^{-2}, resulting in a solidification interface velocity increase from $v_{RS}(t) = v_{RS}(30\mu s)$ = 0.11 m/s to $v_{RS}(67.5\mu s)$ = 0.28 m/s (Fig. 3b). Subsequently, in *Stage II*, 70 μs < t ≤ 107.5 μs, the RS interface accelerated more rapidly, average acceleration a_{II} = 9867 ms^{-2}, from $v_{RS}(t = 70\mu s)$ = 0.31 m/s to $v_{RS}(107.5\mu s)$ = 0.68 m/s (Fig. 3b). In *Stage III*, 107.5 μs, < t ≤ 127.5 μs, an even larger acceleration of the RS interface, a_{III} = 12,500 ms^{-2}, has been determined (Fig. 3b). RS is complete at 127.5 μs < t < 130 μs and the averaged interfacial velocity reaches a maximum of $v_{RS}(t = 127.5\mu s) \approx 0.93$ m/s (Fig. 3b). The initial acceleration of the stagnant solid-liquid interface in *Stage I*, a_i, was much more rapid than during the remainder of the RS microstructure evolution. The first measurable finite solidification interface velocity of 0.11 m/s in *Stage I* having been achieved within 2.5μs, the interframe delay period between successive MM-DTEM images (Fig. 3a, 27.5μs and 30μs delay time), gives a lower limit for a maximum linear velocity increase, i.e., a constant

acceleration, a_i = 0.11/(2.5×10^{-6}) ms^{-2} = 44,000 ms^{-2}. This initial rate of solidification interface velocity change is up to about ten times more rapid than the average interface accelerations during formation of the morphologically distinct RS microstructure in Zones A, B and C, in *Stage I, Stage II* and *Stage III* (Fig. 3), respectively.

Considering the migration of the solidification interface for the duration of *Stage I*, Δt_I=40 µs, at velocities between 0.11 m/s and 0.28 m/s, i.e., at an average velocity of v_I = (½)(0.28+0.11) m/*s* = 0.195 m/ s, gives a first-order estimate for the width of the Zone A microstructure, ΔA, of Δ*A* = v_I * Δt_I = (0.20)(40) µm = 8.0 µm. This is in excellent agreement with the experimental measurements obtained from TEM images (Fig. 3a, Fig. 4a). The migration of the solidification interface at velocities between 0.31 m/s and 0.68 m/s, i.e., at an average velocity of v_{II} = (½)(0.31+0.68) m/*s* = 0.495 m/s for the duration of *Stage II*, Δt_{II}=40 µs, gives an estimate for the width of the Zone B microstructure, Δ*B* = v_{II} * Δt_{II} = 19.8 µm, which is in satisfactory agreement with experimental observation of Δ*B* ≈ 18 µm (Fig. 3a and Fig. 4a). For *Stage III* the average velocity of the solidification rate has been determined as v_{III} = (½) (0.70+0.93) m/*s* = 0.815 m/s (Fig. 3b). Based on solidification interface migration at this average rate for the duration of Δt_{III}≈20µs of *Stage III* in the solidification interface velocity evolution the width of the Zone C region of the RS microstructure of the Al-20Cu alloy can be estimated as ΔC = v_{III} * Δt_{III} = 16.3 µm, which agrees reasonably well with the experimental observation (Fig. 3a and Fig. 4a). Hence, it is concluded that the formation of the three morphologically distinct regions of the RS microstructure of the Al-20Cu alloy, Zone A, Zone B and Zone C, can be attributed to the migration of a solidification interface in the velocity regimes labeled as *Stage I, Stage II*, and *Stage III*, respectively, in Fig. 3. The RS microstructure changes for Zone A, Zone B and Zone C relate to crystal growth mode changes that are associated with distinct regimes of the solidification interface velocity and the solidification interface acceleration [28,33]. Namely, the change from the RS microstructure of Zone A to that of Zone B occurs at v_{I-II} = 0.28 m/s, and for the change from Zone B to Zone C occurs at v_{II-III} = 0.68 m/s (Fig. 3).

3.3. Postmortem characterization of the rapid solidification microstructure

3.3.1. Overall morphology and scale of the distinct microstructure zones

Fig 4a shows a representative BF TEM image overview of the RS microstructure of the Al-20Cu alloy. The morphologically distinct microstructure zones formed by directional RS crystal growth, Zone A, Zone B and Zone C, have been labeled in Fig. 4a. Phase maps and corresponding orientation maps of the RS microstructure of the Al-20Cu alloy obtained by PED-ACOM in the TEM [32], are depicted in Fig. 4b, c, d and e, respectively. The microstructure of the HAZ is partly included in the TEM overview image and the ACOM data at the left-hand side of Fig. 4a, b and c, where equiaxed shape θ-Al_2Cu grains are discernible. The ACOM TEM data of Fig. 4d and e have been obtained from Zone C of the RS microstructure. Examples of nanoscale spatial resolution atomic number density sensitive HAADF STEM imaging and composition mapping by STEM EDXS are shown for the HAZ in Fig. 5, the HAZ at the transition to Zone A of the RS microstructure in Fig. 6, Zone B of the RS microstructure in Fig. 7, and Zone C of the RS microstructure in Fig. 8.

Higher spatial resolution details of the RS microstructure are discussed separately with respect to the solidification interface velocity in subsequent sections (3.3.2, 3.3.3).

The approximate average widths of the distinct RS microstructure zones indicated in Fig. 4a are in good agreement with those measured from the low-magnification MM-DTEM images (Fig. 3a) and consistent with the growth distances that would be expected for migration of the solidification interface at the average velocities and for the durations of *Stage I, Stage II* and *Stage III* determined from the MM-DTEM in-situ experiments (Fig. 3b). It is reasonable to conclude that the RS microstructure Zone A, Zone B and Zone C formed behind a solidification interface migrating at velocities in the regimes defined as *Stage I, Stage II* and *Stage III*, respectively. There is some overlap between the distinct microstructure zones as the RS microstructure transitions from Zone A to Zone B, which is correlated with the solidification interface velocity reaching vI-II = 0.28 m/s, and from Zone B to Zone C for solidification interface velocity reaching vII-III = 0.68 m/s (Fig. 3b and Fig. 4a). The conditions triggering the respective growth mode transitions must have been established at slightly different times or in other words for slightly different distances of crystal growth along the migrating solidification interface at a length scale on the order of about 2 µm. This suggests that the migrating solidification interface was not perfectly aligned with the far-field isotherms resulting from the Gaussian profile of the laser pulse at these transitions in the RS microstructure evolution. Hence, it appears reasonable to propose that segments of the solidification interface may have exhibited an irregular or rough morphology with protrusion into the nominally hotter superheated liquid and adjacent recesses over a length scale of about 2 µm by the time the RS crystal growth facilitated the transitions from the formation of the Zone B to Zone C (Fig. 4a). Such a rough morphology for the RS interface would indicate that solutal effects may have resulted in discernible local growth rate differences.

In the phase maps of Fig. 4b and d locations where the PED patterns matched best with the reciprocal space lattice templates of θ-Al_2Cu, α-Al and θ'-Al_2Cu are shown colored in red, gray, and black, respectively. The HAZ and Zone A of the directionally grown RS microstructure are dominated by θ-Al_2Cu with significant minority area fractions indexed as α-Al (Fig. 4b). The approximate boundaries of Zone A of the RS microstructure, average width of about 8 µm to 8.5 µm, are marked by solid lines in Fig. 4b. Conversely, for Zone B of the RS microstructure the phase map is almost entirely dominated by α-Al with very small regions, presumably intergranular regions, indexed as θ-Al_2Cu (Fig. 4b). The Zone C microstructure (Fig. 4d, e) is dominated by α-Al PED signals. Occasionally isolated nanoscale regions marked as θ'-Al_2Cu are identified in the phase map for the latter parts of Zone B and for Zone C (Fig. 4d). Correlation of the phase maps with the orientation maps from the equivalent areas reveals that the HAZ seeds the growth of the columnar grains in Zone A, since they are continuous across the RS microstructure into Zone B with respect to the α-Al lattice (e.g., compare crystal orientations at boundary between Zone A and Zone B marked by a solid blue line in Fig. 4c). The dramatic switch in the dominant phase identified by the PED assisted ACOM analysis for Zone A, θ-Al_2Cu, and Zone B, α-Al, could originate from changes in the scale and in the morphology of the RS microstructure that correlate with a critical change in the solidification interface velocity as it transitions from *Stage I* to *Stage II* during RS at v_{I-II} = 0.28 m/s (Fig. 3). This has been confirmed by additional postmortem micro-

characterization (e.g., Fig. 6 and Fig. 7, Section 3.3.3). The spatial resolution in the ACOM TEM data of Fig. 4b to 4d is limited by the PED scan step size of 14 nm. Multiple phases may contribute to the PED signal for a given pixel in the scans used to create the phase and orientation maps of Fig. 4, if they overlapped along the electron beam path through the thickness of the crystalline alloy layer, 160 nm. The assignment of the phase shown in the phase maps for a given pixel reflects only the most probable match of the experimental PED pattern with a single phase using the reciprocal space lattice templates for the three phases. The strongest phase specific signal in the PED patterns tends to dominate the successful phase specific indexing. Additional STEM imaging and composition analysis, e.g., Fig. 5 and in Fig. 6, confirmed that the HAZ and Zone A microstructures are comprised of only of θ-Al_2Cu and α-Al. The HAZ contains equiaxed grains of pro-eutectic θ-Al_2Cu and a eutectic constituent of α-Al and θ-Al_2Cu in the nanoscale channels between them (Fig. 5). The Zone A microstructure exhibits eutectic cells with nanoscale lamellae of α-Al and θ-Al_2Cu (Fig. 6). Furthermore, the HAADF STEM image and composition map shown in Fig. 7 for the RS microstructure Zone B illustrates considerable refinement of the scale of the Cu-rich Al_2Cu phase, ≈10–15 nm, and changes in the morphology of the two phases constituting the intragranular features of the eutectic cells grown in *Stage II* relative to those of Zone A, e.g., Fig. 6a. It is therefore reasonable to conclude that the contrast differences discernible in the MM-DTEM images and the dramatic changes in the ACOM phase maps for the Zone A and Zone B of the RS microstructure (Fig. 3, Fig. 4) are correlated with changes in the scale and morphology of the multiphase columnar grains, the eutectic cells, established in *Stage I* and *Stage II* of the solidification interface velocity evolution during RS.

The complex contrast features associated with Zone C of the RS microstructure in the MM-DTEM images are related to the formation of the numerous competitively grown and thus irregularly shaped banded morphology grains (Fig. 4a). Several banded grains spawned at different locations from the columnar morphology grains of Zone B of the RS microstructure and grew competitively until they impinged, forming the Zone C region of the RS microstructure (label X in Fig. 4d, and Fig. 4e). Examples of different banded grains (labels A, B, C, D in Fig. 4a) and several sections of the boundaries between them are marked in Fig. 4a together with the location where the last liquid solidified (label X in Fig. 4a, d and e). Each banded grain represents a single matrix lattice of α-Al and is comprised of alternating bands of single-phase regions of super-saturated α-Al and two-phase regions where θ'-Al_2Cu phase is discontinuously distributed within α-Al (e.g., Fig. 4a, d and e, Fig. 8) [8]. In Fig. 4e a total of nine differently oriented α-Al grains are seen to meet near the location marked by the label X where the last liquid was consumed at the termination of the RS process. The banded grains of Zone C of the RS microstructure of the Al-20Cu alloy formed behind a solidification interface migrating on average at velocities larger than $v_{II\text{-}III}$ = 0.68 m/s (*Stage III*, Fig. 3). The STEM data of Fig. 8 confirms the formation of alternating single-phase and two-phase bands in Zone C of the RS microstructure.

Hence, in the RS microstructure of the hypereutectic Al-20Cu alloy the morphologically distinct Zone A is a eutectic cell regime with a nanoscale lamellar morphology (label θ/α-eutectic, regular lamellar, Fig. 4a), Zone B is a regime of continued columnar grain formation by a growth mode rendering further scale refinement and a non-lamellar or irregular morphology that is

dominated by α-Al as the apparent majority phase or matrix (label α/θ-eutectic, irregular, α-cell like, Fig. 4a), while Zone C is the regime of banded grains, respectively (e.g., Zone A, Zone B, Zone C, Fig. 3 and Fig. 4).

3.3.2. Heat-affected zone microstructure

In contrast to the as-deposited alloy film, the HAZ two-phase microstructure consists of equiaxed θ-Al_2Cu grains that are separated by an intergranular and continuous network of α-Al dominated eutectic product of occasionally nearly regular lamellar but mostly of irregular morphology (Fig. 5). The θ-Al_2Cu crystals have grown from on average diameters of no more than 45 nm in the as-deposited state to about 100 nm average diameter and exhibited compositions in the range of 30.7 at. % Cu to 33.3 at.% Cu (Fig. 5). This is consistent with the composition range for the θ-Al_2Cu phase. The continuous intergranular eutectic network is characterized by a channel width of about 40–80 nm (Fig. 5a and b). The most Cu depleted regions in the HAZ are associated with α-Al phase supersaturated with Cu solute to concentrations of about 11.8 at. % (e.g., location label 9 in Figs. 5a and 4d). For the bright contrast features located in the intergranular eutectic network of the HAZ, which are expected to represent θ-Al_2Cu crystal, the maximum Cu concentrations did not exceed 17.3 at.% Cu. This corresponds approximately to the eutectic composition and is by nearly a factor of two deficient regarding the stoichiometry of the θ-Al_2Cu phase. The large Cu supersaturation of the α-phase and the Cu deficiency measured for the θ-phase in the narrow intergranular eutectic regions would be consistent with the latter being enveloped by the former. The intergranular network of eutectic would be envisaged to form from the liquid in the narrow channels bounded by the adjacent θ-Al_2Cu crystals, which reject Al into the adjacent liquid as they grow. Limits on diffusional composition adjustments due to the small scale and geometry of the liquid channels and the high rate of eutectic solidification interface migration are likely responsible for the mostly irregular morphology of the eutectic presenting in the HAZ of the hypereutectic Al-20Cu alloy. The general morphology and scale of the HAZ observed here for the hypereutectic Al- 20Cu alloy are consistent with formation by solidification of a partially melted region during the *Incubation* period (Fig. 2) [15,24].

3.3.3 Rapid solidification microstructure: Zone A, zone B and zone C

The HAADF STEM image of Fig. 6a shows the HAZ microstructure directly adjacent to Zone A of the RS microstructure. Prior to formation of the Zone A microstructure at the onset of directional RS crystal growth this region represents the location of the stagnant solid-liquid interface established at the end of the *Incubation* period when the partially melted regions solidified to form the HAZ (Fig. 3 and Fig. 4). Zone A of the RS microstructure is comprised of eutectic cells with lamellar morphology (Fig. 6a). Their competitive growth leads to occlusion of some cells by the lateral widening of the more rapidly growing adjacent eutectic cells in the earliest stage of directional RS (Fig. 6a). The growth of the regular lamellar eutectic of the columnar grains or eutectic cells of Zone A was seeded from the eutectic constituent of the intergranular network presenting in the adjacent HAZ microstructure (Fig. 6a). For example, continuous faint contrast associated with the Cu enriched θ-phase in the intergranular eutectic constituent of the HAZ

microstructure can be discerned crossing the equiaxed pro-eutectic θ-Al_2Cu grains marked by the labels X and Y in Fig. 6a. This implies that even the large θ-Al_2Cu grains, e.g., X and Y in Fig. 6a, did not grow through the entire thickness of the Al-Cu alloy layer of the thin film sample. Adjacent to them above or below or both, liquid enriched in Al relative to alloy composition must have existed at the end of their growth to allow for the eutectic from the intergranular regions of the HAZ microstructure to solidify across them. Faint bright contrast features associated with Cu enriched strands cross the Al enriched or conversely Cu depleted layers adjacent to most of the large θ-Al_2Cu grains at the boundary with the lamellar eutectic cells (e.g., near label X, and label Y in Fig. 6a). The compositions measured by STEM EDXS for the field of view shown in Fig. 6a are depicted as a Cu concentration map in Fig. 6b. Compositions measured as averages for several select intergranular regions and regions of a θ-phase grain marked as 1 to 5 in Fig. 6a are summarized in the table of Fig. 6d. The α-Al in the intergranular eutectic regions of the HAZ adjacent to the Zone A of the RS microstructure is Cu solute supersaturated with at minimum 9.7 at.%Cu. The average compositions including both phases presenting in the intergranular eutectic regions ranged from about 12.6 at.% Cu to 16.1 at.% Cu. Except for one of them with 33 at.% Cu, the θ-Al_2Cu grains in the field of view of the STEM data presented in Fig. 6 exhibited composition of about 30 at.% Cu, i.e., slightly deficient in Cu content relative to Al_2Cu stoichiometry, 33.3 at.% Cu. This is consistent with some overlap of the Al enriched (conversely, Cu depleted) regions with the equiaxed θ-Al_2Cu grains. The latter have a higher melting temperature than the Cu depleted (conversely Al enriched) regions that surround them. Therefore, the equiaxed θ-Al_2Cu grains can grow at a higher temperature than the adjacent regions of liquid of Al-enriched composition relative to the alloy.

Line profiles for the composition and image analysis for the lamellar eutectic cells of Zone A of the RS microstructure have been used to determine local changes in the lamellar wavelength, λ. The changes in this microstructural metric can be used to evaluate the local growth rates in Zone A. Under the assumption of diffusion limited growth and a minimal diffusion distance of $x \approx \lambda$ (note, $\lambda/2 \leq x \leq (\pi/2)(\lambda)$, considering the shortest straight line and as longest a semicircular diffusion path) an upper limit for the eutectic growth rate can be estimated. For the location in the intergranular eutectic to the left-hand side of the θ-Al_2Cu grain marked by the label Y in Fig. 6a, i.e., across regions including those marked by numbers 3 and 4 for EDXS averages reported in Fig. 6d, a lamellar wavelength of λ=55 nm has been determined. With the diffusion coefficient of Cu solute diffusion in the liquid state, $D = 4\times10^{-9}$ m^2s^{-1} [34], and using the minimum diffusion distance of $x \approx \lambda$=55 nm this gives an estimated maximum growth rate of $v = D/x = (4\times10^{-9}\ m^2s^{-1}) / (55\times10^{-9}\ m) = 0.07$ m/s. At the very onset of eutectic cell formation in Zone A of the RS microstructure, i.e., next to the Cu depleted regions forming ahead of the largest pro-eutectic θ-Al_2Cu grains observed, the lamellar spacings, λ, range from 30 nm to 28 nm, which implies estimated maximum growth rates for regular lamellar eutectic of 0.13 m/s to 0.14 m/s. For the region marked by the yellow arrow in the lamellar eutectic cell of Zone A of the RS microstructure shown in Fig. 6a composition line profile has been obtained (Fig. 6c) and the lamellar wavelength has been determined as λ = 25 nm, giving $v = 0.16$ m/s. The average lamellar spacings at the right-hand-side of the field of view of Fig. 6a decreases to λ ≈ 18 nm, giving a

maximum growth rate estimate of v = 0.2 m/s. Hence, it can be concluded that the solidification interface velocity almost tripled for the eutectic product from ≈ 0.07 m/s at the transition from the *Incubation* period to *Stage I*, reaching 0.2 m/s during RS directional crystal growth in Zone A over a distance equivalent to the field of view of the STEM micrograph of Fig. 6a, i.e., about 1.2 µm. Notably, the growth rate estimates derived from the lamellar spacings of the eutectic presenting at different locations in Fig. 6a are consistent with the large acceleration of the initially stagnant solid-liquid interface at the onset of directional RS, which has been inferred from the experimentally measured solidification interface velocities in *Stage I* of Fig. 3b, 0.11 m/s ≤ vI = 0.195 m/s ≤ 0.28 m/s, and are associated with the formation of Zone A of the RS microstructure (Fig. 3, Section 3.2). Furthermore, the solidification interface traveling at 0.2 m/s would require about 6 µs to traverse 1.2 µm, which is also consistent with detection of Zone A formation in the in-situ MM-DTEM experiments (Fig. 3). The minimum lamellar spacings that can be supported by diffusion limited coupled growth of the α-Al and θ-Al_2Cu phases of the regular lamellar eutectic of Zone A can be estimated from the maximum solidification interface velocity measured at the end of *Stage I*, i.e., $v_{I\text{-}II}$ = 0.28 m/s (Fig. 3b), as λ ≈ 14 nm. STEM images of the eutectic cells of Zone A of the RS microstructure occasionally exhibited regions with contrast features that would be consistent with a 2λ-mode eutectic, e.g., to the right of the θ-phase grains labeled X and Y in Fig. 6a [29].

Fig. 7 shows a HAADF STEM image and the associated EDXS Cu concentration map obtained from Zone B of the RS microstructure for a location separated by 15 µm from the boundary of Zone A with the HAZ. This area was located near to the middle of the about 18–20 µm wide Zone B of the RS microstructure of the Al-20Cu alloy (e.g., Fig. 4). In contrast to Zone A where a regular lamellar eutectic and in some locations a 2λ-type and optical mode eutectic comprised of α- and θ-phase was observed, here a morphologically modified, non-lamellar or irregular and further scale refined microstructure that is dominated by α-phase was obtained. The coupled growth of the two constituent phases of α-Al (intermediate level of gray contrast in Fig. 7b) and Al_2Cu (brightest contrast in Fig. 6b) present in the eutectic cells of Zone B occurs behind a now quite rapidly migrating solidification interface, 0.31 m/s ≤ v_{II}=0.5 m/s ≤ 0.68 m/s, where v_{II} is an estimate for the average velocity of the solidification interface in *Stage II* (Fig. 3b). At these levels of interfacial migration rate the diffusional processes in the liquid boundary layer adjacent to the newly formed solid cannot maintain a regular lamellar morphology. Instead, an increasingly discontinuous and scale refined Cu rich Al_2Cu phase forms with an irregular, 'seaweed-like' morphology that appears to be embedded within the continuous α-Al for Zone B of the RS microstructure.

The Cu concentrations tabulated in Fig. 7c have been obtained as averages for equal areas, diameters ≈20 nm, from locations in the Cu concentration map of Fig. 7a, e.g., marked by numerals 1 to 6 and small circles in the corresponding STEM image of Fig. 7b. The average composition for the entire map of the field of view of Fig. 7a, 19.9 at.% Cu, corresponds to the alloy composition (Fig. 7c). The compositions of small areas including the θ-Al_2Cu related bright contrast features, labeled 1, 2, 3 and 4, have been found consistently to be slightly more Cu-rich than the alloy with an average of 21.5 at.% Cu (Fig. 7). Conversely, compositions of the small

areas focused on the α-Al phase, e. g., labels 5 and 6, have been found consistently to be slightly Cu depleted with average composition of 16.9 at.% Cu (Fig. 7). Cu solute partitioning is still accomplished during the coupled two-phase growth behavior responsible for formation of Zone B of the RS microstructure. However, the solidification interface velocity increased more than two-fold during formation of the RS microstructure of Zone B, average velocity vII=0.5 m/s, when compared with Zone A, average velocity v_I=0.20 m/s, leading to enhanced solute trapping of Cu in the α-Al phase. Increased solute trapping for the α-Al phase reduces the Cu available to support θ-Al_2Cu phase formation. The θ-Al_2Cu phase with its layered and chemically ordered tetragonal crystal structure has limited potential for accommodating Cu deficient growth. Consequently, a reduction in the fraction of θ-Al_2Cu phase would be expected during growth of the eutectic cells behind an accelerating solidification interface during *Stage I* and *Stage II* of the RS interface velocity evolution (Fig. 3). Qualitatively, inspection of the STEM image of Fig. 7b suggests that the area fraction of the darker gray regions, taken to represent solute supersaturated α-Al phase, is larger than the area fraction of the brighter contrast features representing the Al_2Cu phase and increases as the velocity of the solidification interface increases from left to right of Fig. 7a and b. Using a threshold for Cu concentration in Fig. 7a and for the gray-level of intensity in Fig. 7b as the respective upper limit to delineate Al regions from Al_2Cu regions changes in the area fractions of α-phase have been determined and were found to increase across the field of view (Fig. 7). For example, when selecting 16.9 at.% Cu as the threshold in Fig. 7a, the average α-phase area fraction for the field of view is 55.1%, while the areas marked by blue rectangle outlines at left and right have α-phase area fractions of 51.1% and 58.0%, respectively.

Invoking the continuous growth model (CGM) the lateral width scale, x, of the Cu rich Al_2Cu phase formed during RS behind the solidification interface traveling at velocity v would be expected to be limited by the width, δ, of the liquid diffusion boundary layer adjacent to the solidification interface according to $D/v \approx \delta$ [17]. Hence, akin to the calculation of the lamellar wavelength in diffusion limited formation of lamellar eutectic in Zone A, based on the experimentally determined solidification interface velocity in *Stage II* estimates for the width of the Al_2Cu phase can be derived to be in the range of 13 nm ≤ x ≤ 8 nm for 0.31 m/s ≤ v ≤ 0.68 m/s during formation of Zone B of the RS microstructure. This length scale corresponds reasonably well with the lateral width of the brightest contrast features in the HAADF STEM image of Fig. 7b, with median width of 11 nm to 13 nm. The Zone B microstructures is dominated by α-Al phase while the scale of the Al_2Cu phase refines to the 10 nm range. Changes in the volume fractions of the two phases presenting in the eutectic microconstituent and the refinement of the scale of the Al_2Cu phase are attributed to the enhanced solute trapping in the α-Al solid solution phase or conversely, the difficult and limited solute trapping in the θ-Al_2Cu, as the solidification interface accelerated. The microstructural characteristics of Zone B of the RS microstructure are suitable to rationalize the drastic change from a θ-phase dominated Zone A to an α-phase dominated Zone B observed in the phase map of Fig. 4b. As the scale of the Al_2Cu phase in the eutectic reduces towards the spatial resolution limit of the PED-ACOM data, which cannot be smaller than the 14 nm scan step size, the probability of detecting its presence decreases towards zero.

Fig. 8 shows details of the RS microstructure in Zone C, including for the transition from Zone B to Zone C and of the central region of Zone C where the terminal single-phase bands of several banded grains impinged at the end of the RS process. As the accelerating solidification interface reached a velocity $v = v_{II-III} \approx 0.7$ m/s at the transition from Stage II to Stage III, select grains of Zone B exhibited a change in crystal growth mode (Fig. 3, Fig. 4). The STEM image of Fig. 8a depicts alternating single and two-phase bands characteristic of the banded grains in Zone C [6,28,29]. The width of the two-phase bands tends to decrease while that of the single-phase bands remains approximately constant or gradually increased during banded growth as the average rate of interface migration increased during the RS process (Fig. 8a) [6]. For the hypereutectic Al-20Cu alloy Zone C of the RS microstructure begins with formation of a single-phase band and terminates with a single-phase region of solute supersaturated α-Al (Fig. 8). In Fig. 8b the two-phase microstructure of one eutectic cell in Zone B, label Columnar A, changes characteristically abruptly to the single-phase microstructure of the first single-phase band of the Banded region that defines Zone C, labeled *Partionless band*. The element concentration line scan of the first single-phase band is shown in Fig. 8c. The single-phase bands of Zone C are formed contiguously from the α-Al phase presenting in the two-phase microstructure of select Zone B grains (e.g., label Columnar A, Fig. 8a). As listed in Fig. 8e, for the area marked by a rectangle near label 1 in Fig. 8b the average composition of the single-phase band has been determined as 20.1 at.% Cu, the alloy composition. The single-phase bands are maximally supersaturated α-Al phase (Fig. 8c). The RS microstructure formation in the Al-20Cu alloy transitioned from the regime of coupled two-phase growth in Zone A and Zone B to the regime of single-phase growth for the single-phase bands in banded grains of Zone C. During single-phase band formation the interface velocity reaches and then briefly exceeds the critical value of the velocity of absolute stability, $v_a \approx 0.7$ m/$s \approx v_{II-III}$, and the non-equilibrium partition coefficient, k(v), approaches the limiting value of k(v) = 1 for complete solute trapping. Complete solute trapping is predicted for solidification interface velocity equal to the diffusive speed, v_d, of the Al-Cu alloy, which in the CGM framework can be estimated as $D/a0 \approx v_d \approx 8$ m/s, when $a_0 \approx 0.5$ nm is a length taken to be of similar magnitude as the lattice parameters of the respective phases [35,36].

At the onset of single-phase growth in Zone C, the α-Al crystal that forms the single-phase band can grow more rapidly in directions parallel to the isotherms than normal to the isotherms. The direction normal to the isotherms points radially inward from the perimeter of the melt pool towards its center as marked by a white arrow in Fig. 8a and d, respectively. The very rapid lateral solid growth at local segments of the solidification interface at velocity larger than the maximal solidification interface velocity for two-phase growth in Zone B, $v=v_{II-III}\approx 0.7$ m/s, facilitates occlusion of neighboring Zone B two-phase grains. The occlusion process is illustrated in Fig. 8b where the Zone B grain labeled *Columnar A* undergoes the growth mode transition from coupled two-phase growth to single-phase growth. Its rapid lateral growth stops further growth of its neighbors, e.g., the Zone B grain labeled *Columnar B* (Fig. 8b). The boundary between the first single-phase band of the new banded grain of Zone C of the RS microstructure with the occluded Zone B grains exhibits a narrow layer of eutectic solidification product that presumably formed

from the retained liquid alloy adjacent to the solidification interface during the rapid lateral growth of the Zone B grains (E.g., Fig. 8b and 8c). As the crystal forming the single-phase band grows further into the superheated liquid the solidification interface decelerates and eventually reaches a sub-critical value of the migration rate that drops below the critical value of $v_a \approx 0.7$ m/*s* $\approx v_{II\text{-}III}$ and two-phase growth of α-Al and θ'-Al_2Cu phases establishes a two-phase band in the banded grain. This oscillatory behavior of the solidification interface grows the alternating single- and two-phase bands of the banded morphology grains of Zone C and the occlusion process gives rise to their chevron shape patterns (Fig. 8a and b). Nucleation of the Cu-enriched phase is required in the two-phase bands, which has been shown to favor formation of the θ'-Al_2Cu (Fig. 8a, Fig. 4c, d) [8,15,29, 37].

As shown in the STEM images of Figs. 8d, e and the associated Cu concentration map of Fig. 8f, at the end of the RS process in Zone C single-phase bands of different banded grains meet and the last retained liquid between them forms a narrow boundary with separate Cu-depleted α-Al and Cu-enriched Al_2Cu regions discernible. Fig. 8d shows the last single-phase regions formed at the end of the RS microstructure evolution in the Al-20Cu alloy after laser melting. The labels 1 in Fig. 8a and d mark the same locations and the dominant direction for RS crystal growth, radially inward to the center of the originally formed melt pool, i.e., normal to the far-field isotherms, is marked by white arrows. Along this direction the width of the terminal single-phase bands increased drastically when compared with the almost constant or only gradually increasing width of the single-phase bands formed prior (Fig. 8a and d). For example, as measured along the directions indicated by the white arrows in Fig. 8a and d, the approximate widths of the penultimate and the terminal single-phase band have been determined as 800 nm and 4.2 μm, respectively. This large, approximately five-fold, and stepwise change in the increase of the width for the final single-phase bands when compared with the width changes for the previously formed single-phase regions in the banded grains of Zone C has been observed consistently in the central region of the RS microstructure of the Al-20Cu alloy (e.g., Fig. 4a, Fig. 8d). We posit that it indicates a final growth mode transition from the oscillatory growth mode of the banded growth regime to stable α-phase plane front growth. In prior work using hypereutectic Al-19.3 at%Cu (36 wt.%) and Al-22at.%Cu (40 wt.%) a transition to α-phase plane front growth has been reported to occur for solidification interface velocity of about 1.5 m/s to 2.0 m/s [38]. However, this earlier research was experimentally limited to exploration of solidification interface velocity equal to and smaller than 2 m/s and did not study alloys with Cu concentrations larger than 19.3 at % (36 wt.%) and smaller than 22 at.% (40 wt.%) [38]. Notably, for Al-22at.%Cu (40 wt.%) banded morphology growth has not been observed and the transition to α-plane front growth followed directly from an optical eutectic growth mode rather than from the banded growth, as was the case for the Al-19.3at.% Cu (36 wt.%) alloy [38]. The Al-20Cu (≈37 wt.% Cu) alloy falls into the experimentally unexplored narrow composition range where the critical velocity for the transition from banded to α-phase plane front growth has been predicted to decrease very rapidly with composition, and the interface velocity regime for banded morphology growth shrinks and is expected to disappear [38].

Using the area of the retained liquid determined experimentally from the MM-DTEM in-situ observations for the three image frames at delay time of 122.5 μs to 127.5 μs (Fig. 3a) instantaneous averaged crystal growth rates can be estimated for the final stages of RS. For the 122.5 μs and 125 μs delay time MM-DTEM images the retained areas of liquid are equivalent to circles with effective radii, r_{eff}, of r_{eff} = 5.4 μm (± 1.6 μm) and r_{eff} = 3.3 μm (± 1.6 μm), respectively. In the 127.5 μs MM-DTEM image frame the area is too small to provide a meaningful measurement, giving an effective radius r_{eff} = 1.3 μm (± 1.6 μm). The error stated corresponds to single pixel resolution in the digitally recorded individual MM-DTEM image frames (Fig. 3). Considering completion of RS at 127.5 μs the average for a linear growth rate in the final stage of RS microstructure evolution over the duration of 2.5 μs can be estimated as v = (3.3 μm/2.5μs) = 1.3 m/s with a conservative lower and upper error limit of 0.7 m/s and 2.0 m/s, respectively. The transition from Zone B to Zone C has been determined to ensue for a solidification interface velocity of $v_{II\text{-}III} = v_a$ = 0.7 m/s. The transition from banded to α-phase plane front growth has been reported for an interface velocity of 2.0 m/s with a lower limit of 1.5 m/s for Al-19.3Cu (36 wt.%) and is predicted to decrease with increased Cu fraction for the hypereutectic Al-Cu alloys [38]. For the Al-22Cu (40 wt.%) the transition from eutectic growth of optical 1λ-mode eutectic to α-phase planar growth has been predicted for solidification interface velocity just below 2 m/s [e.g., 3, 38]. Hence, it is reasonable to propose a transition from the banded growth mode regime to the stable α-phase plane front growth regime for the Al-20Cu alloy for a solidification interface velocity $v_{PF} > v_a$ = 0.7 m/s and v_{PF} < 2.0 m/s, which would be consistent with the estimated magnitude of v_{PF} = 1.3 m/s based on the in-situ MM-DTEM experiments performed here. Notably, the linear dimension of the central region of Zone C constituting the α-phase plane front growth regime related RS microstructure in the Al-20Cu alloy, i.e., radii ≈ 4 μm, is consistent with the retained liquid area observed at the end of the RS process in the MM-DTEM in-situ experiments.

The last solid formed in terminal single-phase bands and on average across the boundary between different banded grains of Zone C of the RS microstructure exhibited the alloy composition, as shown in Fig. 8f and h, and listed in Fig. 8g. The final single-phase bands formed during the alloy RS exhibit Cu concentration variations on the order of 4 at.% Cu at length scales of about 10 nm (Fig. 8f). This is consistent with the magnitude of the non-equilibrium partition coefficient, k(v), approaching very close to but not reaching unity, k(v) < 1, even for the solidification interface migrating on average with a velocity, v_{PF} = 1.3 m/s and no larger than 2.0 m/s, in the α-phase plane front growth regime. Within the conceptual framework of the CGM lateral diffusion ahead of the solid alloy forming in the α-phase plane front regime is limited to dimension $x = D/v_{PF} = 4\times10^{-9}\ m^2s^{-1}/1.3\ ms^{-1}$ = 3 nm, where D is the Cu solute diffusion coefficient in the liquid alloy [14,17], which is smaller than the observed ≈10 nm scale for variations of Cu solute concentrations on the order of 4 at.% in the α-Al solid solution of the terminal single-phase regions (Fig. 8f). We attribute the observed Cu solute lateral micro-segregation developed during the early stages of the α-phase plane front growth regime at average interface velocity v_{PF} = 1.3 m/*s* > v_a = 0.7 m/s, i.e., in the regime of absolute interfacial morphological stability, to nano-scale and unstable morphological perturbations at the solidification interface. These small wavelength perturbations are envisaged to occur spontaneously, persist for short durations at a given

segment of interface and develop local curvature at the migrating solidification interface [39]. Even small and temporary perturbations of the time averaged flat interface morphology result in local variations of the interface velocity and thus the local solute rejection rate to the adjacent liquid. This provides a mechanism for locally establishing lateral micro- or nano-segregation without the need for lateral diffusion as the non-equilibrium solute partition coefficient varies with interface velocity and therefore locally along the solidification interface.

3.4 Solidification interface velocity, supercooling and crystal growth modes

The solidification microstructure forming after the laser irradiation induced melting of the hypereutectic Al-20Cu alloy exhibited the HAZ and the directional RS microstructure with Zone A, Zone B and Zone C (Fig. 2, Fig. 4). Formation of these distinct solidification microstructure zones is correlated to the four distinguishable stages observed for the evolution of the on average increasing velocity of the solidification interface, labeled in Fig. 3 as *Incubation, Stage I, Stage II* and *Stage III*, respectively. For cooling conditions that to good approximation permit full adjustments of composition at the solid-liquid interface the solidification of superheated liquid hypereutectic Al-20Cu alloy would establish a microstructure comprised of a primary constituent of pro-eutectic θ-Al_2Cu and a secondary constituent of regular lamellar (θ/α)-eutectic (e.g., schematically depicted in Fig. 9) [27]. As the temperature, T, traverses the solidification range, $T_{\theta\text{-liq}} = 839\ K \leq T \leq T_{eut} = 821$ K, solidification would start with growth of the pro-eutectic θ-Al_2Cu, while the retained liquid adjusts composition according to the θ-phase liquidus from 20 at.% Cu towards the eutectic composition, ≈17 at.%Cu, as the fraction of solid increases (Fig. 9). Under near-equilibrium conditions the Al-20Cu alloy solidification would be complete once all retained liquid has transformed to lamellar eutectic for an approximately isothermal stage at temperatures just slightly below the eutectic isotherm, T_{eut}. Under geometric constraint with directional heat extraction the resulting directional solidification would establish a microstructure of elongated cellular or dendritic morphology pro-eutectic θ-Al_2Cu with lamellar eutectic in the inter-cellular or inter-dendritic regions. Due to the thin film geometry constraint the directional solidification after the pulsed laser irradiation melting of the Al-20Cu thin films studied here is associated with very large cooling rates on the order of 106 K/s. This is consistent with the experimentally observed durations for the solidification process of ≈ 100 μs (Fig. 3) and estimates for cooling of the superheated alloy melt by ≈ 500 K from peak temperatures of at least ≈ 1300 K to at least the eutectic temperature, T_{eut}=821 K [24]. Hence, conditions at the solidification interface are driven far away from equilibrium and local equilibrium cannot be maintained.

As the solidification interface migration velocity increases and interfacial conditions are driven farther away from equilibrium, increased localization of diffusion gives rise to increased levels of solute trapping, scale refinements and morphological modifications of the solid constituents in the RS microstructure of the Al-20Cu alloy (Figs. 4–8). Interface stability analysis for alloy solidification into a positive thermal gradient, a superheated melt, for an accelerating solidification interface velocity predicts changes in the morphology of the stable interface sections from initially planar to cellular, then from cellular to dendritic and dendritic to cellular,

and finally from cellular to planar front growth [3]. Concomitantly, with the solidification interface velocity increase the temperature at the interface, T_i, decreases, i.e., the interfacial supercooling, $\Delta T_i = T_{eq}-T_i$, where T_{eq} is the equilibrium liquidus temperature, increases for cellular and dendritic growth. For the plane front single-phase growth regime at the highest interface velocities the interfacial temperature increases again with increased interface velocity due to kinetic attachment and interfacial curvature effects [3,31,37]. According to the continuous growth model (CGM) the competitively selected crystal growth mode during formation of the RS microstructure in the Al-20Cu alloy will change as the interface velocity and related interface temperature change [17]. The selected active crystal growth mode will be the one that can maintain the highest interfacial temperature at the given interface velocity. In concentrated multicomponent alloys, such as the binary hypo- and hyper-eutectic Al-Cu alloys, multiphase microstructures develop during RS involving modes of cellular and/or dendritic growth of the respective primary pro-eutectic α-Al or θ-Al_2Cu phases, eutectic growth, and the plane front growth of the respective pro-eutectic α-Al or θ-Al_2Cu phases [31]. The evolution of the interface temperature with interface migration velocity for the Al-20Cu alloy has been calculated for the relevant growth modes using the models and methods developed in prior research by Aziz, Trivedi and Kurz et al. [40–42]. Details related to the calculations of the velocity dependence of the solidification interface temperature for the different growth modes accessible during RS of the Al-20Cu alloy are summarized in the Appendix. The active growth modes, ranges of respective interface velocity, and estimates for interfacial temperature associated with the formation of the different zones of the solidification microstructure observed here for the hypereutectic Al-20Cu alloy after laser melting are summarized schematically in the graphics of Fig. 9.

Consistent with prior studies for hypoeutectic Al-Cu alloys containing between 4 at.% Cu and about 11 at.% Cu the HAZ forms from the partially melted hypereutectic Al-20Cu alloy during the *Incubation* stage prior to onset of the directional RS processes (Fig. 3, Fig. 5) [8,15]. Due to the spatiotemporal resolution limitations of the MM-DTEM experiments the details of the solidification interface velocity during the incubation stage could not be determined from the in-situ imaging (Fig. 3). However, the total duration of 28 µs and an upper limit of the maximum growth rate for the secondary constituent of eutectic in the HAZ of 0.07 m/s have been determined from postmortem analysis (Fig. 2 to Fig. 6a, Section 3.3.3). As the solidification interface temperature, T, enters and sweeps through the equilibrium solidification range, from $T_{\theta\text{-}liq} = 839\ K \leq T \leq T_{eut} = 821$ K, during the *Incubation* period of the solidification interface velocity evolution the primary phase of pro-eutectic θ-Al_2Cu forms by a dendritic growth mode (θ-dendrite, Fig. 9). The spatial thermal gradient reduces during *Incubation,* and eutectic constituent forms between the θ-phase grains at reducing distances behind the θ-phase dendrite tip. A steep solidus and T0-line of the θ-Al_2Cu phase imply a steep increase in the interfacial supercooling as the solidification interface velocity increases since the capacity for solute trapping at the accelerating solidification interface is very limited (Fig. 9) [31]. Moreover, the layered chemically ordered crystal structure of the θ-Al_2Cu phase results in a tendency for a facetted structure of the solidification interface which also imposes limits on the crystal growth rate and growth mechanism [39,43,44]. An effect of these characteristics of the θ-phase and its solidification

interface is the limitation of the regime of dendritic growth of the pro-eutectic constituent forming during directional RS of the hypereutectic alloy.

Notably, at the boundary between the HAZ and Zone A of the RS microstructure eutectic cells appear to emanate from the HAZ as directional RS starts in *Stage I* (Fig. 4, Fig. 6). In contrast, for hypoeutectic alloys of Al-4Cu, Al-7Cu, Al11Cu (all in at.%) the pro-eutectic α-Al solid solution crystals are the first directional RS products and attain appreciable Cu supersaturation, e.g., up to about 8 at.% Cu in Al- 11Cu alloy due to the copious solute trapping during growth of elongated columnar grains in a microstructural transition zone behind the accelerating solidification interface [8,15,24]. After MM-DTEM laser melting the morphological transition from plane front to cellular/dendritic growth at the beginning of RS have been detected for α-Al solid solution crystals in Al-11Cu prior to the relatively stable growth of α-cells [8]. Such a microstructural transition zone, where elongated grains form and the pro-eutectic θ-phase exhibits increased solute trapping as the solidification interface velocity increases, has not been detected in the RS microstructure of the hypereutectic Al-20Cu alloy. With reference to Fig. 6a, which depicts several θ-phase grains at the boundary with the eutectic cells of Zone A of the RS microstructure a minor elongation of some of these grains along the horizontal diameters relative to their vertical diameters can be detected, which represents a deviation from the equixially shaped θ-phase grains typical of the HAZ. For example, taking the grain marked by the label Y in Fig. 6a, its vertical diameter is 240 nm and its horizontal diameter is 320 nm, giving an estimate for the limit of the length for directional crystal growth (horizontal direction) of the pro-eutectic θ-phase of 80 nm. Taking these deviations from a circular cross-section as a metric provides an upper limit estimate of the spatial extend for the region where RS crystal growth was dominated by dendritic growth of θ-phase of 80 nm to 100 nm during RS of the Al-20Cu alloy (e.g., Fig. 6a). Since θ-phase dendritic growth is replaced by eutectic cell growth at the onset of Zone A microstructure formation the upper limit for the dendritic growth rate must be smaller than the maximum growth rate of the lamellar eutectic in the HAZ, which has been estimated as 0.07 m/s from the minimum lamellar wavelength observed (E.g., Fig. 6). This appears reasonable as calculations performed here for the interface temperature changes with interface velocity for Al-20Cu predict a transition from θ-phase dendrites to eutectic growth for a solidification interface velocity of 0.038 m/s and associated interfacial undercooling by 12 K from 821 K in equilibrium to 809 K (Fig. 9a). This agrees well with results of analogous calculations previously reported for Al-22at.% Cu (40 wt.% Cu) [31]. If the maximum growth velocity of θ-dendrites is taken as 0.04 m/s, at most 2.5 μs would elapse during formation of 100 nm of new solid. Due to the spatiotemporal resolution limitations of the MM-DTEM imaging experiments, Δx = 1.6 μm and Δt = 2.5μs, this process would not be detectable and therefore is neglected in the solidification interface velocity evolution plotted in Fig. 3b. Hence, in the schematic summary presented in Fig. 9b and Fig. 9c the θ-phase dendrite growth regime is limited to the HAZ formation during *Incubation*.

A first crystal growth mode transition is observed from that of θ-dendrites to eutectic growth for solidification interface velocity on the order of 0.04 m/s to 0.07 m/s based on the interface temperature calculations and the experiments performed here. The magnitude of this first growth mode transition velocity is below the smallest velocity that could be measured via

the in-situ observations of the migrating solidification interface in the MM-DTEM experiments for *Stage I* of the solidification interface velocity, which is associated with the formation of the eutectic cells of Zone A (Fig. 6a, Fig. 9). For solidification interface velocities in the range of *Stage I*, 0.11 m/*s* < $v_I \leq$ 0.28 m/s, and *Stage II*, 0.30 m/*s* < $v_{II} \leq$ 0.68 m/s, the regular lamellar eutectic of Zone A and the non-lamellar, irregular eutectic of Zone B formed via eutectic growth modes and an α-phase dominated dendritic mode, respectively (Fig. 9). We attribute the change in the morphology and scale of the eutectic observed for Zone A to that characteristic of the RS microstructure of Zone B to the limitations imposed on the coupled zone growth of θ- and α-phase by the characteristics of the chemically ordered intermetallic θ-phase. Since the capacity for solute trapping is very limited for θ-phase, maintaining crystal growth requires the rejection of significant fractions of Al atoms from the alloy liquid in the boundary layer back into the bulk liquid. This can be considered as a solute drag effect and would be expected to reduce the effective driving force for continued solid growth, resulting in a reduced effective solidification interface velocity for the θ-phase [18]. Conversely, the comparable ease for solute trapping of the α-Al solid solution phase implies a smaller magnitude of solute drag effects and therefore ability for more rapid crystal growth of the associated atomically rough solid-liquid interface at the larger interfacial supercooling (see Section 3.3.3). As the solidification interface accelerates during the eutectic growth regime of *Stage I* and during *Stage II*, the interfacial supercooling and the solute trapping in the α-Al phase increase, while the volume fraction of Al_2Cu phase decreases accordingly (Fig. 3, Fig. 9). This is consistent with rapidly decreasing slope of the metastable extension of the non-equilibrium solidus of the α-Al phase and the essentially constant and large slope of the metastable extension of the θ-phase solidus [8,31]. We posit here that the solidification interface acceleration change at the transition from *Stage I* to *Stage II* and the associated change in the RS microstructure from the regular lamellar eutectic of Zone A to the irregular non-lamellar morphology of Zone B can be attributed to the more significant effects of solute drag on the growth of the θ-phase than for the α-Al phase (Fig. 9). Further solidification velocity increase during growth in *Stage II* while forming Zone B microstructure reduces the interfacial temperature towards the α-phase T0-line (Fig. 9a and Fig. 9b). At this maximum supercooling of the solidification interface a change to α-phase plane front growth occurred for a critical solidification interface velocity $v_{II\text{-}III} \approx v_a \approx$ 0.7 m/s. This third growth mode change is responsible for the formation of the single-phase bands of the banded grains in Zone C of the RS microstructure of the hypereutectic Al-20Cu alloy for Stage III in the interface velocity evolution (Fig. 9).

The results of numerical calculations comparing interfacial temperatures as a function of interface velocity for dendritic growth, eutectic growth, and plane front growth of the α- and θ-phases in the hypereutectic Al-20Cu alloy akin to those reported previously for concentrated Al-Cu alloys in the vicinity of eutectic compositions in [31] are shown in Fig. 9a. Based on these calculations the CGM predicts growth mode changes for hypereutectic Al-20at%Cu (37 wt.%Cu), from first, θ-dendrites to (θ/α)-eutectic at relatively modest RS interface velocities of 0.04 m/s and associated interface temperature of $T_i \approx$809 K. A second growth mode transition from (θ/α)-eutectic to α-dendrites, i.e., α-cell growth, is predicted for interface velocity of 0.21 m/s at 738

K, followed by a third, from α-dendrites to α-phase plane front growth, i.e., for the start of banded grain formation, at about 0.69 m/s and $T_i \approx 735$ K (Fig. 9a). The experiments performed here showed that the change from cellular and/or dendritic growth of θ-phase to eutectic cell growth at the transition of the HAZ to Zone A of the RS microstructure of the hypereutectic Al-20at.%Cu (37 wt.%Cu) occurred for solidification interface velocity in the range of 0.05 m/$s \leq v <$ 0.11 m/s (Fig. 3, Fig. 6). The interface velocity for the change from the eutectic of microstructure Zone A to that of the irregular morphology and α-phase dominated RS microstructure Zone B has been determined as 0.28 m/s while the average velocity for Zone A RS microstructure during Stage I was determined as 0.2 m/s (Fig. 3 and Fig. 9b). The change of growth mode to α-phase plane front growth at the boundary between Zone B and Zone C of the RS microstructure of the hypereutectic Al-20at.%Cu occurred for v = 0.7 m/s (Fig. 9b). Hence, the experimentally determined velocities for the growth mode transitions associated with the morphological changes observed as Zones A, B and C in the RS microstructure and the growth mode velocities predicted by the interface temperature calculations performed here show reasonable to good agreement.

Most of the area of the Zone C of the RS microstructure was established by banded growth (Fig. 4, Fig. 8). The banded growth involves an oscillatory behavior for the conditions at the solidification interface with single-phase bands growing when the interface velocity $v = v_i \geq v_a =$ 0.7 m/s, while the two-phase bands form when $v = v_i < v_a$ due to the deceleration of the interface in response to the effects of the positive thermal gradient and attachment kinetic effects reducing the interfacial supercooling [37] (Section 3.3.3,Fig. 8). The formation of the central region of Zone C, accounting for a region with an approximate radius of 4 μm or about 20% of the 20 μm radius of the entire Zone C of the RS microstructure of the Al-20Cu alloy has been attributed to stable a-phase plane front growth (Section 3.3.3, Fig. 8). This final growth mode transition was not detectable in the MM-DTEM in-situ experiments and therefore has not been incorporated in the solidification interface velocity evolution graph reported in Fig. 3b. However, based on the postmortem analyses of the microstructural characteristics of the central region of Zone C it has been concluded that it formed behind solidification interface segments that migrated at velocities $v = v_i \geq v_a = 0.7$ m/s, on average reaching $v_i = v_{PF} = 1.3$ m/s, which is reported here as velocity for transition from the banded growth regime to the α-phase planar front, v_{PF} (Section 3.3.3, Fig. 8, Fig. 9). This final transition of the growth modes responsible for the RS microstructure evolution in the Al-20Cu alloy is marked schematically as part of the Zone C microstructure regime, with respect to estimated interfacial temperatures and interface velocity in Fig. 9. However, it should be noted that the graphic of Fig. 9b is only a schematic summary useful for illustration purposes, and that the interfacial supercooling is predicted to reduce, primarily due to attachment kinetic effects as the solidification interface velocity continues to increase in the α-phase plane front growth regime (Fig. 9a), while Fig. 9c summarizes the sequence of growth mode transitions proposed here for RS of the Al-20at.%Cu alloy as the interface velocity increases [3].

The experimental results reported here for the Al-20Cu alloy (37 wt. %Cu) establishes experimentally determined ranges of the solidification interface velocity for the different growth

mode regimes responsible for the formation of the morphologically distinct regions of the RS microstructure of hypereutectic Al-20Cu and the critical velocities for the transitions between them (Fig. 9c). These are consistent with previous reports that the growth modes responsible for the solidification microstructure evolution in the hypereutectic Al-20Cu alloy changed with increasing solidification interface velocity from θ-phase dendritic growth to regular lamellar θ/α-eutectic and 2λ- and 1λ-mode eutectic (labeled as θ/α-eutectic in Zone A, Fig. 9c), then to an irregular, α-phase dominated morphology akin to that associated with α-cell growth in hypoeutectic Al-Cu alloys (labeled as α-dominated eutectic or α-cell in Zone B, Fig. 9c). The growth mode responsible for Zone B genesis transitioned to banded growth, and finally α-phase plane front growth at further increased interface velocity (labeled as Zone C, Fig. 9c) in Al- 20Cu (37 wt.%) studied here, while banded growth was not reported for Al-22Cu (40 wt.% Cu) [28–31,37,38]. For Al-19.3Cu (36 wt.% Cu) the additional growth mode transitions from eutectic growth to α-cell growth and then to banded growth have been reported [31,38]. This adds credence to the feasibility of α-cell growth mode being responsible for the formation of the Zone B in the RS microstructure in the Al-20Cu alloy and would be consistent with the results of the solidification interface temperature calculations (Fig. 9a). Compared with the Al-22Cu alloy our experiments on Al-20Cu determined larger values for the transition velocities for the first transition from θ-phase dendritic growth to the regular lamellar θ/α-eutectic growth regime with $v_i \leq v_\theta = 0.07$ m/*s* ≈ 0.1 m/s, i.e., for the onset of Zone A microstructure formation, and for the transition to banded growth, i.e., the transition from Zone B to Zone C microstructure formation, $v_{II\text{-}III} = 0.7$ m/s [38]. Hence, compared to earlier studies of RS microstructure formation in hypereutectic Al-Cu alloys after surface remelting our experiments suggest an extension of the θ-dendrite regime to slightly larger interface velocities at the onset of stage I, $v_i = v_\theta \leq 0.07$ m/*s* ≈ 0.1 m/s (Fig. 9), a transition from the eutectic growth regime from Zone A to Zone B, i.e., to α-cell growth, for $v_{I\text{-}II} = 0.28$ m/s, then to banded growth for $v_{II\text{-}III} \approx 0.7$ m/s, and α-phase plane front growth for $v_{PF} \approx 1.3$ m/s (Fig. 9) [38]. The experimental results of the current study provide previously unavailable estimates for the velocity for the final transition from the oscillatory regime of banded growth to the regime of stable α-phase plane front growth for the Al-20Cu (37 wt.%) alloy (Fig. 9). Given the not insignificant level of uncertainty regarding several assumptions required for the numerical calculations for the RS growth mode behaviors of the hypereutectic Al-20at.%Cu performed here (Fig. 9a, Appendix) and also for analogous calculations previously published for Al-22at.%Cu it is reasonable to propose that estimates for the associated interfacial temperatures for the growth mode transitions observed here experimentally in the hypereutectic Al-20at.%Cu alloy and noted for illustrative purposes only in Fig. 9 are reasonable [31]. The sequence of growth mode changes determined in the current work indicates that α-cell growth prior to transition to banded growth is still feasible for alloys of Cu-richer composition than Al-19at.%Cu (36 wt.%Cu) and the banded growth regime disappears for hypereutectic Al-Cu alloys containing Cu fractions larger than 20 at.% Cu (37 wt.%Cu).

The experimental results presented in the current paper for the hypereutectic Al-20at.%Cu confirm the previously proposed asymmetry of the regime for eutectic growth, the coupled zone for θ- and α-phase, during RS of Al-Cu [31]. Relative to hypoeutectic alloys in the

vicinity of the eutectic composition, where the pro-eutectic α-Al can exhibit significant solute trapping under RS conditions in the dendritic growth mode regime, for hypereutectic alloys the regime for θ-phase dendritic growth is restricted to small solidification interface velocities, while the regime for eutectic growth extends to increasingly hypereutectic compositions as the RS interface temperature decreases for increasing interface velocity (Fig. 9). The experimentally determined solidification interface velocity values and associated RS microstructure characteristics reported here provide data for parts of a previously experimentally unexplored range of hypereutectic alloy compositions where strongly composition sensitive changes in crystal growth mode selection are predicted for solidification microstructure evolution in the Al-Cu system and are suitable to support validation and evaluation of computational model predictions.

Summary and conclusions

Using pulsed laser melting of thin film specimens, the development of the rapid solidification microstructure in hypereutectic Al-20at.%Cu (37 wt.%Cu) has been studied by in-situ MM-DTEM imaging and postmortem TEM/STEM analyses. The active growth modes responsible for the formation of four morphologically distinct regions/zones of the multi-phase rapid solidification microstructure and the respective solidification interface velocity regimes have been determined. A heat affected zone (HAZ) formed from a partially melted region prior to the onset of directional rapid solidification during an initial period of *Incubation*. The rapid solidification microstructure formed by epitaxial growth behind an accelerating solidification interface that migrated with an average velocity of $v_{ave} \approx 0.44$ m/s. The microscale spatiotemporal resolution in-situ MM-DTEM experiments revealed three different regimes for the evolution of the solidification interface velocity, v(t), during rapid solidification, namely, *Stage I, Stage II*, and *Stage III*. Each regime was characterized by a different constant acceleration and average interface velocity, namely, $v_I = 0.20$ m/s, $v_{II} = 0.50$ m/s, and $v_{III} = 0.83$ m/s, for *Stage I, Stage II*, and *Stage III*, respectively. As the initially stationary solidification interface accelerated a very narrow region of pro-eutectic θ-Al_2Cu developed, then significant regions of eutectic cells in Zone A evolved and transitioned to α-phase dominated morphology of Zone B, followed by evolution of banded morphology grains in Zone C. Evidence for single-phase α-Al phase growth was observed in the final stage of rapid solidification process. The first crystal growth mode transition from θ-dendrites to eutectic growth occurred for small magnitudes of solidification interface velocity on the order of $v_{\theta\text{-}e} = v \approx 0.07$ m/s. Subsequently, the initially eutectic growth regime involved two morphologically distinct regions, Zone A with regular lamellar eutectic and Zone B with non-lamellar/irregular morphology akin to α-cells. Zone A formed for solidification interface velocities, v, in *Stage I*, 0.11 m/*s* < *v* = $v_I \leq 0.28$ m/s, and Zone B in *Stage II*, 0.30 m/*s* < *v* = $v_{II} \leq 0.68$ m/s, giving a value of $v_{I\text{-}II} \approx 0.3$ m/s for the transition in morphology of the eutectic cells to that of α-cells. The transition to α-phase plane front growth was responsible for the change to the banded growth regime in Zone C and occurred for solidification interface velocity of $v_{II\text{-}III} \approx 0.7$ m/s . The RS microstructure of Zone C formed in solidification interface velocity *Stage III*, 0.7 m/*s* = $v_a \leq v = v_{III} = 0.83$ m/*s* < 1.3 m/s. The unique characteristics of the central region of Zone C of

the rapid solidification microstructure have been rationalized by invoking a third and final growth mode transition from banded growth to the true a-phase planar front regime for a critical velocity of $v = v_{PF} = 1.3$ m/s.

Cellular/dendritic growth of the θ-Al_2Cu phase was found to be limited to small solidification interface velocities, $v < v_{\theta\text{-}e} = v \approx 0.07$ m/ s. This has been attributed to a low tolerance for solute trapping and associated strong solute drag effects for θ-phase dendrite growth during rapid solidification. As a result, eutectic cell and banded morphology grain regions dominated the rapid solidification microstructure of the hypereutectic Al-20Cu alloy. This confirms an asymmetrically enhanced extension of the eutectic growth regime for hypereutectic Al-Cu alloys when compared with their hypoeutectic counterparts. Unlike in hypoeutectic Al-Cu, where extended regimes of α-cell growth generate columnar morphology grains, the equivalent growth mode transitions for θ-phase growth are suppressed in hypereutectic Al-Cu due to the kinetic advantage offered by the transition to eutectic growth. The rapid solidification microstructure evolution sequences observed here for hypereutectic Al-20at.%Cu (37 wt.%Cu) are qualitatively consistent with those reported for the Cu-richer composition of hypereutectic Al- 19.3at.%Cu (36 wt.%Cu) alloy [37,38]. The quantitative experimental measurements of solidification interface velocity and associate nano-scale resolved microstructural details reported here are suitable to support theoretical model development and validation of predictions from computer simulation of rapid solidification microstructure evolution in concentrated Al-Cu alloys of hypereutectic compositions.

Declaration of competing interest

The authors declare that they have no known competing financial interests or personal relationships that could have appeared to influence the work reported in this paper.

Acknowledgments

The research activities at the University of Pittsburgh received support from the National Science Foundation, Division of Materials Research, Metals & Metallic Nanostructures program through Grants No. DMR 1105757 and DMR 1607922. Work at Lawrence Livermore National Laboratory (LLNL) was performed under the auspices of the U. S. Department of Energy, by LLNL under Contract No. DE-AC52–07NA27344. Activities and personnel at LLNL were supported by the U.S. Department of Energy, Office of Science, Office of Basic Energy Sciences, Division of Materials Science and Engineering under FWP SCW0974. The authors acknowledge R. Williams and F. Scheltens of CEMAS at the Ohio State University for assistance with performing the STEM EDXS mapping and initial precursory data analyses.

Appendix

Calculations of the principal interface response functions, namely, the non-equilibrium solute partition coefficient, k(V)=k_v, and the interface temperature, $T_i(V, X_i)$, where V is the interface velocity and X_i the concentration of solute species, i, have been performed for the phase specific relevant growth modes of dendritic, eutectic and plane-front growth in the Al-20at.%Cu alloy. These calculations are based on theory and models developed for dilute alloys, have been applied to hypereutectic Al-Cu previously, and are described in ([45–51]. The calculations support the discussion of our experimental observations of the microstructural morphology and scale, and measurements of the local solidification interface velocity evolving during rapid solidification of the hypereutectic Al-20at.%Cu alloy after pulsed laser melting. Solute trapping was modeled using the theory and model developed by Aziz [46]. Here the non-equilibrium partition coefficient, k(V), is a function of solidification velocity (V) via the relation:

$$\boldsymbol{k(V)} = \frac{\boldsymbol{k_e}+\frac{\boldsymbol{V}}{\boldsymbol{V_D}}}{\boldsymbol{1}+\frac{\boldsymbol{V}}{\boldsymbol{V_D}}} \tag{1}$$

where $\boldsymbol{V_D}$ is a diffusive speed for solute atoms across the solid/liquid interface at a given alloy composition, $\boldsymbol{C}_0$ and growth velocity, **V**. For metals that establish an atomically rough solid-liquid interface during crystal growth a simple relationship for estimating the magnitude of the diffusive speed, $\boldsymbol{V_D}$, is given as $\boldsymbol{V_D} = \boldsymbol{D/a}$, where D is the diffusion coefficient for solute in the liquid at the melting temperature and *a* is a distance on the order 0.5 nm to 5 nm, i.e., in the range of one to ten times the magnitude of the unit cell length dimension. For the Al-Cu alloys with Do=1.06×10^{-7} m^2/s and *Q* = 24 kJ/mole for Cu diffusion in liquid Al, and thus *D* = 3.5×10^{-9} m^2/s at 845 K, this gives for *a* = 0.5 nm the magnitude of 6.96 m/s for the diffusive speed. Prior reports proposed a value of 6.7 m/s for the diffusive speed in Al-Cu alloys for alpha-phase based solidification growth during RS [47,49]. According to Aziz, Trivedi, and Kurz et al. [46–48] the temperature of the tip of a dendrite, T_d, can be determined by [3]:

$$\boldsymbol{T_d} = \boldsymbol{T_m} - \boldsymbol{\Delta T_l} - \boldsymbol{\Delta T_c} - \boldsymbol{\Delta T_r} - \boldsymbol{\Delta T_k} \tag{2}$$

and

$$\Delta \boldsymbol{T_l} = \boldsymbol{m_l(V)C_0}, \Delta \boldsymbol{T_c} = -\boldsymbol{m_l(V)(C_{l*} - C_0)}, \Delta \boldsymbol{T_l} = \frac{\boldsymbol{2\Gamma}}{\boldsymbol{R}}, \text{and } \boldsymbol{\Delta T_k} = \frac{\boldsymbol{V}}{\boldsymbol{\mu_k}} \tag{3}$$

where $\boldsymbol{T_m}$ is the melting temperature of the pure component, $\boldsymbol{C_{l*}}$ is the concentration of solute for the liquid at the tip of the dendrite, and **R** is the dendrite tip radius [49]. The velocity-dependent liquidus slope is determined by [45]:

$$\boldsymbol{m_l(V)} = \boldsymbol{m_l}\left(\boldsymbol{1} + \frac{\boldsymbol{K_e - K(V) + K(V)\ln\frac{K(V)}{K_e}}}{\boldsymbol{|1-K_e|}}\right) \tag{4}$$

Calculations reported in the literature typically used models developed for the dilute end of a binary system for which the equilibrium partition coefficient, K_e, and liquidus slope, m_l, are positive and smaller than unity, $0 < K_e < 1$, and negative, $m_l < 0$, respectively. In an A-B eutectic system these conditions approximately apply to the A-rich regime or the hypoeutectic alloys with A as the solvent and B as the solute if the respective liquidus and solidus are within reasonable approximation straight lines. In the hypereutectic section for the A-B alloys, the situation is different when considering B as solute. For alloys in the hypereutectic range, the value of the equilibrium partition coefficient exceeds one, $K_e > 1$, and the liquidus slope is positive, $m_l > 0$, with respect to the species B. For the Al-Cu system in the composition range from Al to Al_2Cu alloys of hypoeutectic and hypereutectic composition exist in these Al-rich alloys where A=Al is the solvent and B=Cu is the solute. For conditions of RS where the interface velocity is sufficiently large to affect solute trapping in the solid the solidification range reduces with increased velocity. Hence, as the solidification velocity, v, increases during RS, the liquidus slope should increase for the hypereutectic alloy A-B, e.g., for the hypereutectic regime of the Al-Cu alloy system between pure Al and Al_2Cu. Consequently, with respect to the equations used for the calculations of the interface temperature for hypoeutectic Al-Cu alloys, we use a modified expression to determine the velocity-dependent non-equilibrium liquidus slope for the hypereutectic regime as follows:

$$\boldsymbol{m_l(V) = m_l\left(1 + \frac{K_e - K(V) + K(V)\left(-\ln\frac{K(V)}{K_e}\right)}{|1 - K_e|}\right)} \tag{5}$$

This addresses the required consistency with the equilibrium phase diagram and it captures at least qualitatively correctly the effects of the increased interface velocity during RS on the liquidus predicted by thermodynamics for the hypereutectic alloys.

The expression for $\boldsymbol{C_{l^*}}$ is given by [50]:

$$\boldsymbol{C_{l^*} = \frac{C_0}{1 - [1 - k(V)\mathrm{Iv}(P)]}} \tag{6}$$

where $\boldsymbol{Iv(P)}$ is Ivantsov's solution, and $\boldsymbol{P = VR/2{*}D}$ is the Péclet number. $\Delta\boldsymbol{T_I}$ is the undercooling of the alloy with respect to the pure element, $\Delta\boldsymbol{T_c}$ gives the undercooling caused by the build-up of solute ahead of the dendrite tip, $\Delta\boldsymbol{T_r}$ is the undercooling due to the curvature of the dendrite tip, and $\Delta\boldsymbol{T_k}$ is the undercooling due to the attachment kinetics. R not only influences $\Delta\boldsymbol{T_r}$, but also $\Delta\boldsymbol{T_c}$ by affecting the Péclet number. The relationship of R on V has been determined from the report by Gill et al. on scanned laser surface melting induced solidification experiments on hypoeutectic Al-Cu alloy [49]. The R values predicted at different velocities are shown in Fig. A1. These R(v) values for the dendrite tip radius variation with RS interface velocity have been determined for α-phase dendritic growth.

The determination of a solution for the eutectic growth mode requires the coupling of the solute undercooling to the curvature undercooling of each phase [47]:

$$T_e = T_E - \Delta\bar{T}_k - \Delta\bar{T}_s - \Delta T_c^{\alpha} - \Delta T_r^{\alpha} = T_E - \Delta\bar{T}_k - \Delta\bar{T}_s - \Delta T_c^{\theta} - \Delta T_r^{\theta} \quad (7)$$

The model developed by Gill et al. [3] for the coupled eutectic growth of α- and θ-phase in Al-Cu assumed equal sums for contribution from interfacial free energy and curvature related behavior for the two phases involved in the formation of the regular eutectic, i.e., $-\Delta T_c^{\alpha} - \Delta T_r^{\alpha} = -\Delta T_c^{\theta} - \Delta T_r^{\theta}$. In Eq. (7), ΔT_c is the solute undercooling, ΔT_r is the curvature undercooling and ΔT_k captures the influence of attachment kinetics. The influence of the solute trapping can be determined by [51]:

$$\Delta\bar{T}_s = \frac{K(V)\Delta T_0 \mathrm{Iv}(P)}{1-[1-K(V)]\mathrm{Iv}(P)} \quad (8)$$

and ΔT_0 is the interface velocity dependent solidification range, which can be determined by:

$$\Delta T_0 = \frac{m_l(V)c_0|K(V)-1|}{K(V)} \quad (9)$$

For the planar front α phase growth mode the temperature will be lowered by attachment kinetics at high velocities under steady state growth condition, while under non-steady state conditions the planar front interface temperature will increase due to the increase in the effective solidus temperature [51]. For the planar front growth mode the interface temperature can be determined by [51]:

$$T_i = T_s + \left(\frac{m_l^{\alpha}(V)}{K^{\alpha}(V)} - \frac{m_l}{K_e}\right) C_0 - \frac{V}{\left(\frac{V_o \Delta S_{\alpha}}{R_g T_m}\right)} \quad (10)$$

where T_s is the equilibrium solidus temperature of the alloy.

Values of key thermophysical parameters used in the calculations of the growth mode dependent interface response function calculations performed here for Al-20at.%Cu are collated in Table 1. In Table 1, the values for $m_{l\text{-}\alpha}$ and $k_{e\text{-}\alpha}$ listed for α-phase have been used in the α-phase related calculations of the interfacial temperature as function of interface velocity for the hypereutectic Al-20Cu alloy. These values have been determined from the metastable extensions of the solidus and liquidus calculated for Al-Cu and reported in prior work [47,49]. These values of the non-equilibrium liquidus slope and solute partition coefficient differ from those applicable for the more dilute composition Al-Cu alloys in the hypoeutectic range, i.e., for Cu concentrations ≤ 10wt%Cu [47,49]. We justify the selection of these values from the non-equilibrium extensions of the metastable phase diagram because for solute concentration in the hypereutectic regime the slopes of the liquidus and solidus lines of the alpha phase differ significantly from those of the more dilute sections in the hypoeutectic part of the metastable phase diagram [47,49]. In particular, the slope of the solidus becomes very flat for Cu concentrations ≥ 20 wt%Cu. Therefore, we used the larger values for the liquidus slope and K values, $m_{l\text{-}\alpha}$ and $k_{e\text{-}\alpha}$ (Table 1),

to calculate the interface temperature evolution with interface velocity for a-phase dendritic growth (Fig. 9a above). Additionally, when calculating the $T_i(V)$-profile associated with the θ-phase growth, the diffusive velocity, $V_D = V_D(\theta) = 0.7$ m/s, has been used, which is an estimate stated in prior publications to be reasonable [47,49]. This research argued that the value to be used for V_D in calculations of the interface response functions for θ-phase is reduced by about an order of magnitude relative to that of α-phase, $V_D(\alpha)$=6.7 m/s, since the growth interface is not nearly perfectly atomically rough, as is the case for nearly perfect example of metallic material behavior exhibited by a-phase [47]. References referred to in the text of this Appendix are listed below for convenience.

Fig. A2 shows the principal results of the calculations for the change in growth mode dependent interface temperature with interface velocity, the $T_i(V)$-plots, for Al-20at.%Cu. The growth modes considered include θ-phase dendritic, a-phase dendritic, (θ/α)-eutectic, and α-phase plane front mode, respectively. The results summarized in Fig. A2 have been adapted as Fig. 9a into the main text.

References

[1] S. Gorsse, C. Hutchinson, M. Gouné, R. Banerjee, Additive manufacturing of metals: a brief review of the characteristic microstructures and properties of steels, Ti-6Al- 4V and high-entropy alloys, Sci. Technol. Adv. Mater. 18 (1) (2017) 584–610, https://doi.org/10.1080/14686996.2017.1361305.

[2] M.E. Glicksman, Principles of Solidification: An Introduction to Modern Casting and Crystal Growth Concepts, Springer, New York, 2011, https://doi.org/10.1007/ 978-1-4419-7344-3.

[3] W. Kurz, R. Trivedi, Rapid solidification processing and microstructure formation, Mater. Sci. Eng. A 179–180 (1) (1994) 46–51, https://doi.org/10.1016/0921-5093 (94)90162-7. PARTMay.

[4] W. Kurz, D.J. Fisher, R. Trivedi, Progress in modelling solidification microstructures in metals and alloys: dendrites and cells from 1700 to 2000', Int. Mater. Rev. 64 (6) (2019) 311–354, https://doi.org/10.1080/ 09506608.2018.1537090.

[5] Q. Lei, B.P. Ramakrishnan, S. Wang, Y. Wang, J. Mazumder, A. Misra, Structural refinement and nanomechanical response of laser remelted Al-Al_2Cu lamellar eutectic, Mater. Sci. Eng. A 706 (2017) 115–125, https://doi.org/10.1016/j. msea.2017.08.105. August.

[6] J.T. McKeown, et al., In situ transmission electron microscopy of crystal growth-mode transitions during rapid solidification of a hypoeutectic Al–Cu alloy, Acta Mater. 65 (2014) 56–68, https://doi.org/10.1016/J.ACTAMAT.2013.11.046. Feb.

[7] J.T. McKeown, et al., Time-resolved *in situ* measurements during rapid alloy solidification: experimental insight for additive manufacturing, JOM 68 (3) (2016) 985–999, https://doi.org/10.1007/s11837-015-1793-x.

[8] V. Bathula, C. Liu, K. Zweiacker, J. McKeown, J.M.K. Wiezorek, Interface velocity dependent solute trapping and phase selection during rapid solidification of laser melted hypo-eutectic Al-11at.%Cu alloy, Acta Mater. 195 (2020) 341–357, https:// doi.org/10.1016/j.actamat.2020.04.006.

[9] E.J. Lavernia, T.S. Srivatsan, The rapid solidification processing of materials: science, principles, technology, advances, and applications, J. Mater. Sci. 45 (2) (2010) 287–325, https://doi.org/10.1007/s10853-009-3995-5.

[10] R. Zhong, A. Kulovits, J.M.K. Wiezorek, J.P. Leonard, Four-zone solidification microstructure formed by laser melting of copper thin films, Appl. Surf. Sci. 256 (1) (2009) 105–111, https://doi.org/10.1016/J.APSUSC.2009.07.084. Oct.

[11] A. Kulovits, R. Zhong, J.M.K. Wiezorek, J.P. Leonard, Electron microscopy of geometrically confined copper thin films after rapid lateral solidification, Thin Solid Films 517 (13) (2009) 3629–3634, https://doi.org/10.1016/J. TSF.2008.11.132. May.

[12] Y. Liu, M. Liu, L. Luo, J. Wang, C. Liu, The solidification behavior of AA2618 aluminum alloy and the influence of cooling rate, Materials 7 (12) (2014) 7875, https://doi.org/10.3390/MA7127875. Basel.

[13] C. Brito, H. Nguyen-Thi, N. Mangelinck-No¨el, N. Cheung, J.E. Spinelli, A. Garcia, Cellular-to-dendritic and dendritic-to-cellular morphological transitions in a ternary Al-Mg-Si alloy, IOP Conf. Ser. Mater. Sci. Eng. 529 (1) (2019), 012018, https://doi.org/10.1088/1757-899X/529/1/012018. May.

[14] W.W. Mullins, R.F. Sekerka, Stability of a planar interface during solidification of a dilute binary alloy, J. Appl. Phys. 35 (2) (1964) 444, https://doi.org/10.1063/ 1.1713333. Jul.
[15] K.W. Zweiacker, C. Liu, M.A. Gordillo, J.T. McKeown, G.H. Campbell, J.M. K. Wiezorek, Composition and automated crystal orientation mapping of rapid solidification products in hypoeutectic Al-4 at.%Cu alloys, Acta Mater. 145 (2018) 71–83, https://doi.org/10.1016/j.actamat.2017.11.040.
[16] Galenko, S. Sobolev, Local nonequilibrium effect on undercooling in rapid solidification of alloys, Phys. Rev. E 55 (1) (1997) 343, https://doi.org/10.1103/ PhysRevE.55.343. Jan.
[17] M.J. Aziz, T. Kaplan, Continuous growth model for interface motion during alloy solidification, Acta Metall. 36 (8) (1988) 2335–2347, https://doi.org/10.1016/ 0001-6160(88)90333-1.
[18] C.A. Hareland, G. Guillemot, C.A. Gandin, P.W. Voorhees, The thermodynamics of non-equilibrium interfaces during phase transformations in concentrated multicomponent alloys, Acta Mater. 241 (2022), 118407, https://doi.org/ 10.1016/J.ACTAMAT.2022.118407. Dec.
[19] D.R. Gunasegaram, I. Steinbach, Modelling of microstructure formation in metal additive manufacturing: recent progress, research gaps and perspectives, Metals 2021 11 (9) (2021) 1425, https://doi.org/10.3390/MET11091425. Page111425, Sep.
[20] T. Pinomaa, J.M. McKeown, J.M.K. Wiezorek, N. Provatas, A. Laukkanen, T. Suhonen, Phase field modeling of rapid resolidification of Al-Cu thin films, J. Cryst. Growth 532 (2020), 125418, https://doi.org/10.1016/j. jcrysgro.2019.125418.
[21] S. Kavousi, M. Asle Zaeem, Quantitative phase-field modeling of solute trapping in rapid solidification, Acta Mater. 205 (2021), 116562, https://doi.org/10.1016/J. ACTAMAT.2020.116562. Feb.
[22] S. Kavousi, B.R. Novak, J. Hoyt, D. Moldovan, Interface kinetics of rapid solidification of binary alloys by atomistic simulations: application to Ti-Ni alloys, Comput. Mater. Sci. 184 (2020), 109854, https://doi.org/10.1016/J. COMMATSCI.2020.109854. Nov.
[23] T. LaGrange, B.W. Reed, D.J. Masiel, Movie-mode dynamic electron microscopy, MRS Bull. 40 (1) (2015) 23–28, https://doi.org/10.1557/mrs.2014.282.
[24] K. Zweiacker, et al., Determination of crystal growth rates during rapid solidification of polycrystalline aluminum by nano-scale spatio-temporal resolution in situ transmission electron microscopy, J. Appl. Phys. 120 (5) (2016), https:// doi.org/10.1063/1.4960443.
[25] B. Vishwanadh, J. Jo, C.S. Bonifacio, J.M.K. Wiezorek, Site-specific preparation of plan-view samples with large field of view for atomic resolution STEM and TEM studies of rapidly solidified multi-phase AlCu thin films, Mater. Charact. 189 (2022), 111943, https://doi.org/10.1016/J.MATCHAR.2022.111943. Jul.
[26] P. Jreidini, T. Pinomaa, J.M.K. Wiezorek, J.T. McKeown, A. Laukkanen, N. Provatas, Orientation gradients in rapidly solidified pure aluminum thin films: comparison of experiments and phase-field crystal simulations, Phys. Rev. Lett. 127 (20) (2021), 205701, https://doi.org/10.1103/PHYSREVLETT.127.205701/ FIGURES/4/MEDIUM. Nov.
[27] J.L. Murray, The aluminum-copper system, Int. Met. Rev. 30 (1) (2013) 211–233, https://doi.org/10.1179/imtr.1985.30.1.211.

[28] M. Zimmermann, M. Carrard, W. Kurz, Rapid solidification of Al-Cu eutectic alloy by laser remelting, Acta Metall. 37 (12) (1989) 3305–3313, https://doi.org/ 10.1016/0001-6160(89)90203-4. Dec.
[29] S.C. Gill, W. Kurz, Rapidly solidified Al||Cu alloys-I. Experimental determination of the microstructure selection map', Acta Metall. Mater. 41 (12) (1993) 3563–3573, https://doi.org/10.1016/0956-7151(93)90237-M. Dec.
[30] W. Kurz, P. Gilgien, Selection of microstructures in rapid solidification processing, Mater. Sci. Eng. A 178 (1–2) (1994) 171–178, https://doi.org/10.1016/0921-5093 (94)90538-X. Apr.
[31] S.C. Gill, M. Zimmermann, W. Kurz, Laser resolidification of the Al-Al_2Cu eutectic: the coupled zone, Acta Metall. Mater. 40 (11) (1992) 2895–2906, https://doi.org/ 10.1016/0956-7151(92)90454-M. Nov.
[32] E.F. Rauch, M. Véron, Automated crystal orientation and phase mapping in TEM, Mater. Charact. 98 (2014) 1–9, https://doi.org/10.1016/J. MATCHAR.2014.08.010. Dec.
[33] G. Li, et al., Exploiting the rapid solidification potential of laser powder bed fusion in high strength and crack-free Al-Cu-Mg-Mn-Zr alloys, Addit Manuf 47 (2021), 102210, https://doi.org/10.1016/J.ADDMA.2021.102210. Nov.
[34] Y. Du, et al., Diffusion coefficients of some solutes in fcc and liquid Al: critical evaluation and correlation, Mater. Sci. Eng. A 363 (1–2) (2003) 140–151, https:// doi.org/10.1016/S0921-5093(03)00624-5. Dec.
[35] W. Kurz, D. Fisher, Fundamentals of solidification: 4th reised editionRetrospective Collection 35 (1998).
[36] M.R. Rappaz, J.A. Dantzig, Solidification: -Revised & Expanded, EPFL Press, 2016.
[37] M. Carrard, M. Gremaud, M. Zimmermann, W. Kurz, About the banded structure in rapidly solidified dendritic and eutectic alloys, Acta Metall. Mater. 40 (5) (1992) 983–996, https://doi.org/10.1016/0956-7151(92)90076-Q.
[38] S.C. Gill, W. Kurz, Rapidly solidified Al||Cu alloys-II. Calculation of the microstructure selection map', Acta Metall. Mater. 43 (1) (1995) 139–151, https:// doi.org/10.1016/0956-7151(95)90269-4. Jun.
[39] W.J. Boettinger, S.R. Coriell, R.F. Sekerka, Mechanisms of segregation-free solidification, in: Proceedings of the Third Conference on RS Processing, 1982, pp. 45–55. R. Mehrabian, Ed., Gaithersburg, Maryland: Dec.
[40] M.J. Aziz, Model for solute redistribution during rapid solidification, J. Appl. Phys. 53 (2) (1982) 1158–1168, https://doi.org/10.1063/1.329867. Feb.
[41] S.C. Gill, W. Kurz, Rapidly solidified A1–Cu alloys–II . calculation of the microstructure selection map, Acta Metall. Mater. 43 (1) (1995) 139–151.
[42] R. Trivedi, P. Magnin, W. Kurz, Theory of eutectic growth under rapid solidification conditions, Acta Metall. 35 (4) (1987) 971–980, https://doi.org/ 10.1016/0001-6160(87)90176-3.
[43] R. Hamar, C. Lemaignan, Facetting behaviour of Al_2Cu during solidification, J. Cryst. Growth 53 (3) (1981) 586–590, https://doi.org/10.1016/0022-0248(81) 90143-3. Jun.

[44] Z. Song, O.V. Magdysyuk, T. Sparks, Y.L. Chiu, B. Cai, Revealing growth mechanisms of faceted Al_2Cu intermetallic compounds via high-speed synchrotron X-ray tomography, Acta Mater. 231 (2022), 117903, https://doi.org/10.1016/J. ACTAMAT.2022.117903. Jun.
[45] W.J. Boettinger, S.R. Coriell, MICROSTRUCTURE FORMATION IN RAPIDLY SOLIDIFIED ALLOYS, NATO ASI Series, Series E: Applied Sciences (114) (1986) 81–108, https://doi.org/10.1007/978-94-009-4456-5_5/COVER.
[46] M.J. Aziz, Model for solute redistribution during rapid solidification, J Appl Phys 53 (2) (Feb. 1982) 1158–1168, https://doi.org/10.1063/1.329867.
[47] S.C. Gill, W. Kurz, RAPIDLY SOLIDIFIED A1–Cu ALLOYS–II . C A L C U L A T I O N OF THE M I C R O S T R U C T U R E SELECTION MAP, Acta metallurgica et materialia 43 (1) (1995) 139–151.
[48] R. Trivedi, P. Magnin, W. Kurz, Theory of eutectic growth under rapid solidification conditions, Acta Metallurgica 35 (4) (1987) 971–980, 10.1016/ 0001–6160(87)90,176–3.
[49] S.C. Gill, M. Zimmermann, W. Kurz, Laser resolidification of the Al-Al_2Cu eutectic: The coupled zone, Acta Metallurgica et Materialia 40 (11) (Nov. 1992) 2895–2906, 10.1016/0956–7151(92)90,454-M.
[50] H. BILONI, W.J. BOETTINGER, SOLIDIFICATION, Physical Metallurgy (Jan. 1996) 669–842, 10.1016/B978–044,489,875–3/50,013–2.
[51] R. Trivedi and W. Kurz, “Dendritic growth,” vol. 39, no. 2, 1994.
[52] O. Zobac, A. Kroupa, A. Zemanova, K.W. Richter, Experimental Description of the Al-Cu Binary Phase Diagram, Metall Mater Trans A Phys Metall Mater Sci 50 (8) (Aug. 2019) 3805–3815, 10.1007/S11661–019–05,286-X/FIGURES/8.
[53] Y. Du, et al., Diffusion coefficients of some solutes in fcc and liquid Al: critical evaluation and correlation, Materials Science and Engineering: A 363 (1–2) (Dec. 2003) 140–151, 10.1016/S0921–5093(03)00,624–5.
[54] Z. Xue, S. Hu, D. Zuo, W. Cai, D. Lee, K.A. Elijah, Molten pool characterization of laser lap welded copper and aluminum, J Phys D Appl Phys 46 (49) (Nov. 2013) 495-501, 10.1088/0022-3727/46/49/495,501.

Figures

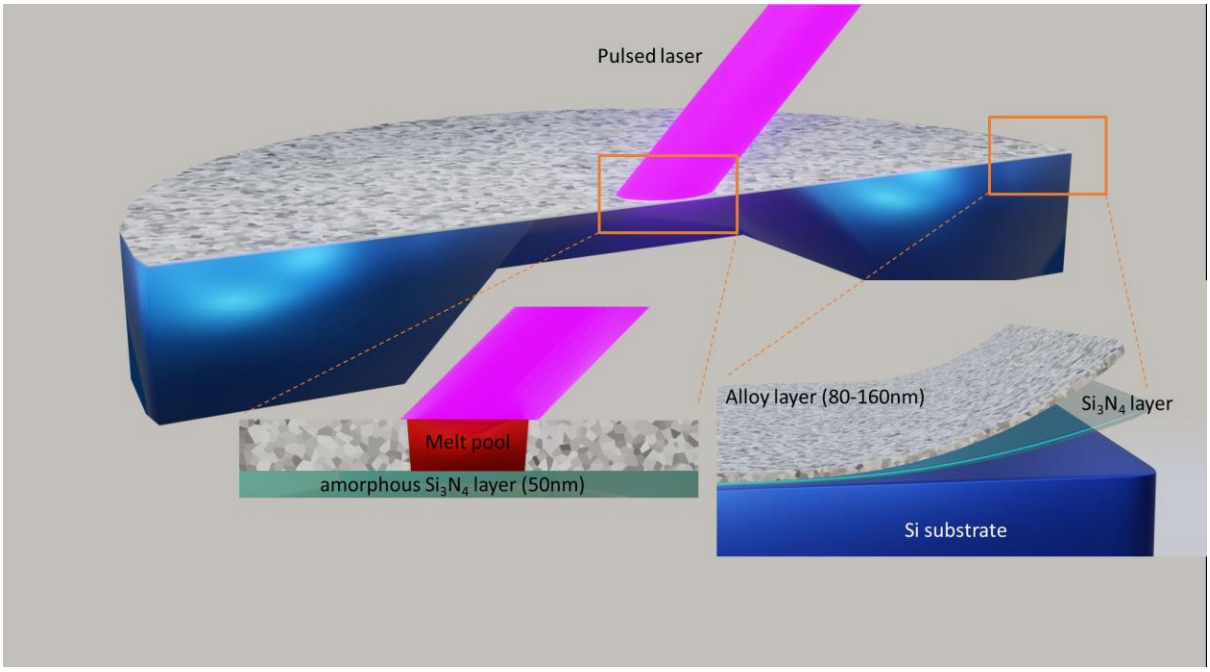

Fig. 1: Alloy thin film specimen setup for MM-DTEM in-situ experiments of rapid solidification after laser pulse melting.

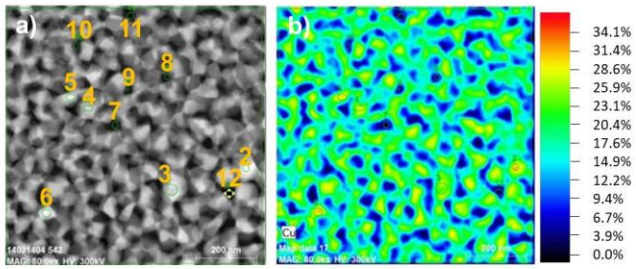

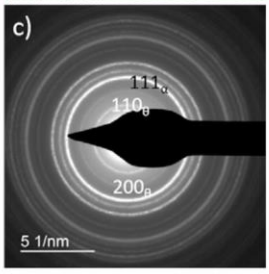

d)

Location	at%Cu	Location	at%Cu
1(view)	20.16	7	2.77
2	35.33	8	3.59
3	29.41	9	3.23
4	31.84	10	5.54
5	36.05	11	3.41
6	35.76	12	3.62

Fig. 2: Microstructure, composition, grain size, and morphology of Al-20at%Cu thin film of as-deposited state: a) ADF STEM image. Numbered and encircled regions correlate with compositions tabulated in d). b) Pseudo-color map of Cu concentration for same area as imaged in a), with a color scale from 0 to 35 at%. c) SADP pattern from a large field of view (≈10µm diameter) of the as-deposited film. Prominent diffraction rings are indexed with α-Al and θ-Al_2Cu phases. d) Average Cu compositions determined by EDXS measurements for the entire field of view and several encircled areas marked by numbers in a).

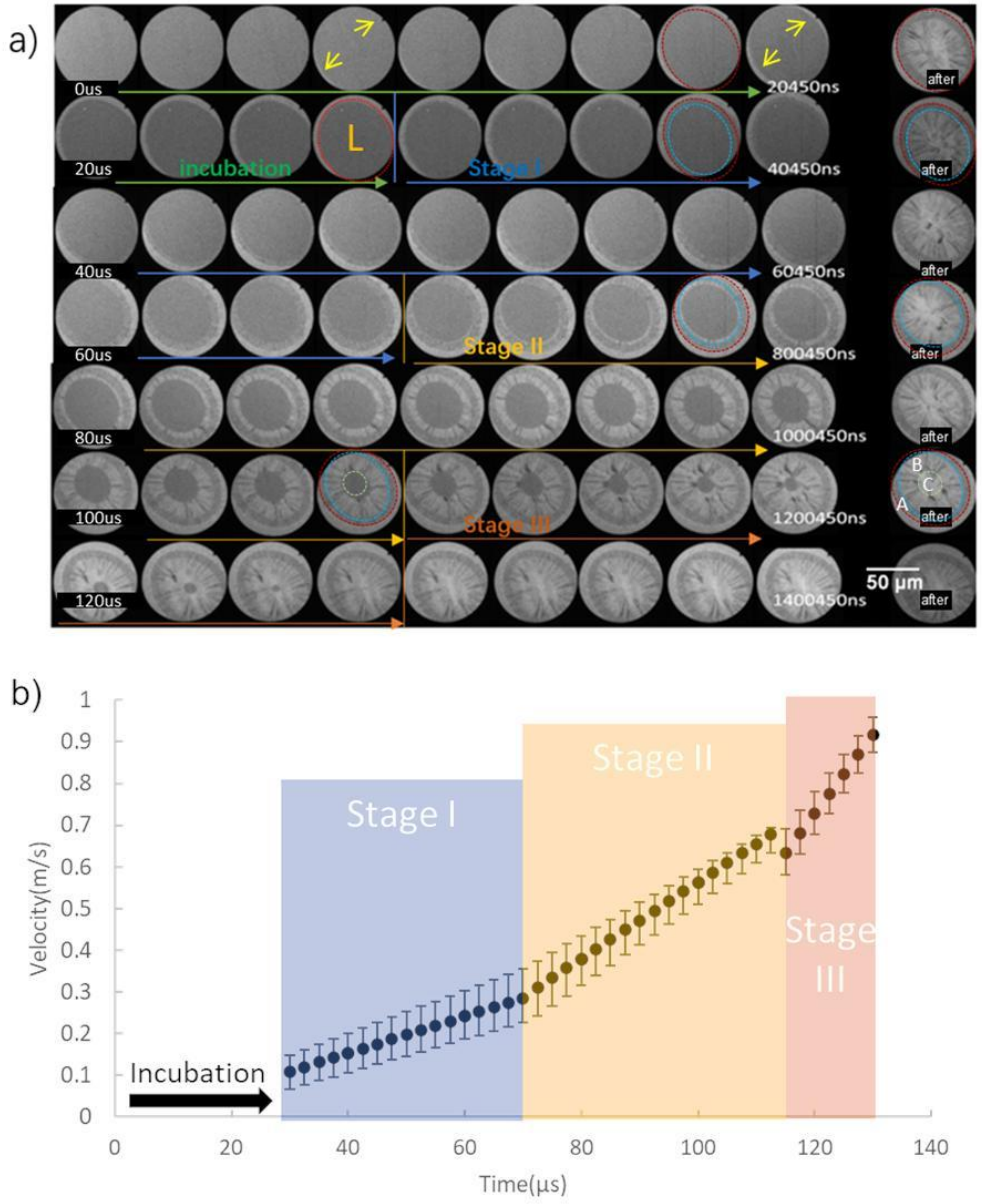

Fig. 3: a) In-situ MM-DTEM bright field image series acquired at different delay times, marked as 0 µs, 20µs, 40µs, 60µs, 80µs, 100µs, and 120µs. Label L in 4th image of the 20µs delay time MM-DTEM series represents liquid phase. The distinct zones of the RS microstructure, Zone A, Zone B and Zone C, are marked as A, B and C in the 'after-image' of the 100µs delay time MM-DTEM series. The yellow (see online version for color) arrows in the fourth and ninth images of the 0µs MM-DTEM image series mark identical locations near the developing HAZ microstructure during the incubation period (see text for more details). The elliptical dashed lines colored in red delineate the maximum extent of the RS microstructure established by directional crystal growth, while cyan- and yellow-colored dashed lines delineate the RS microstructure Zone A from Zone B, and Zone B form Zone C, respectively (see online version for color). b) Plot of the solid-liquid interface velocity as a function of time after the application of pulsed laser irradiation for melting

determined from MM-DTEM image series in a). The incubation period and three stages with different accelerations of the solid-liquid interface are marked as Incubation, Stage I, Stage II and Stage III, respectively.

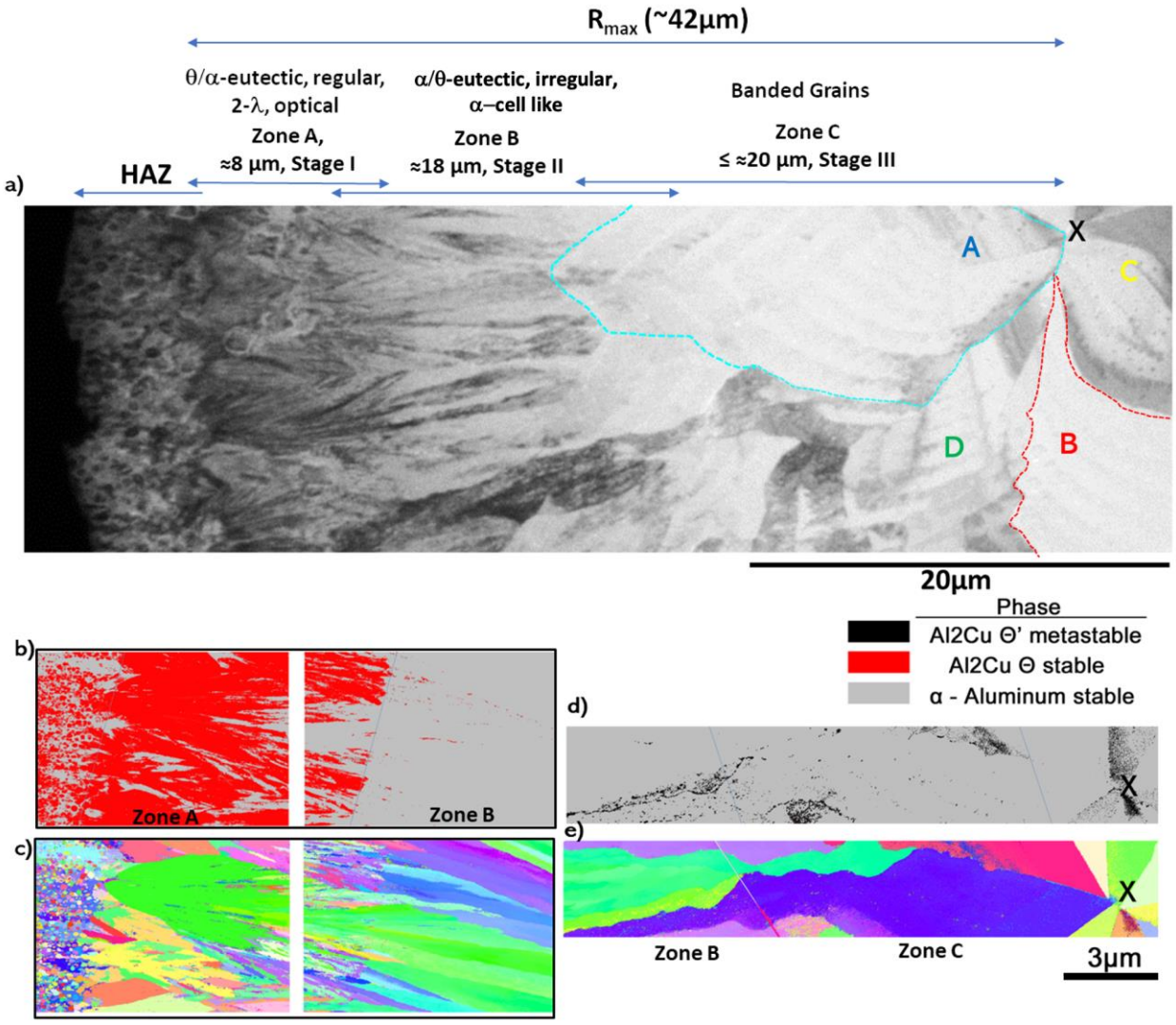

Fig. 4: a) Bright field TEM overview of the RS microstructure with the morphologically distinct regions of Zone A, Zone B, Zone C, and parts of the heat affected zone (HAZ) at left-hand-side. Directional RS crystal growth was approximately horizontal from HAZ at left towards central location marked by letter X. Letters A, B, C and D mark different grains in the banded morphology region of Zone C of the RS microstructure. Blue arrows indicate the approximate width of the morphologically distinct Zone A (θ/α-eutectic), Zone B (α/θ-eutectic, irregular a-cell like) and Zone C (banded grains). b) and d) ACOM TEM phase maps with θ'-Al_2Cu as black, θ-Al_2Cu as red, and α–Al as grey. c) and e) associated ACOM TEM orientation maps. The scale marker in e) is 3 µm and is the same for b) to e). See text for additional details (color in online version).

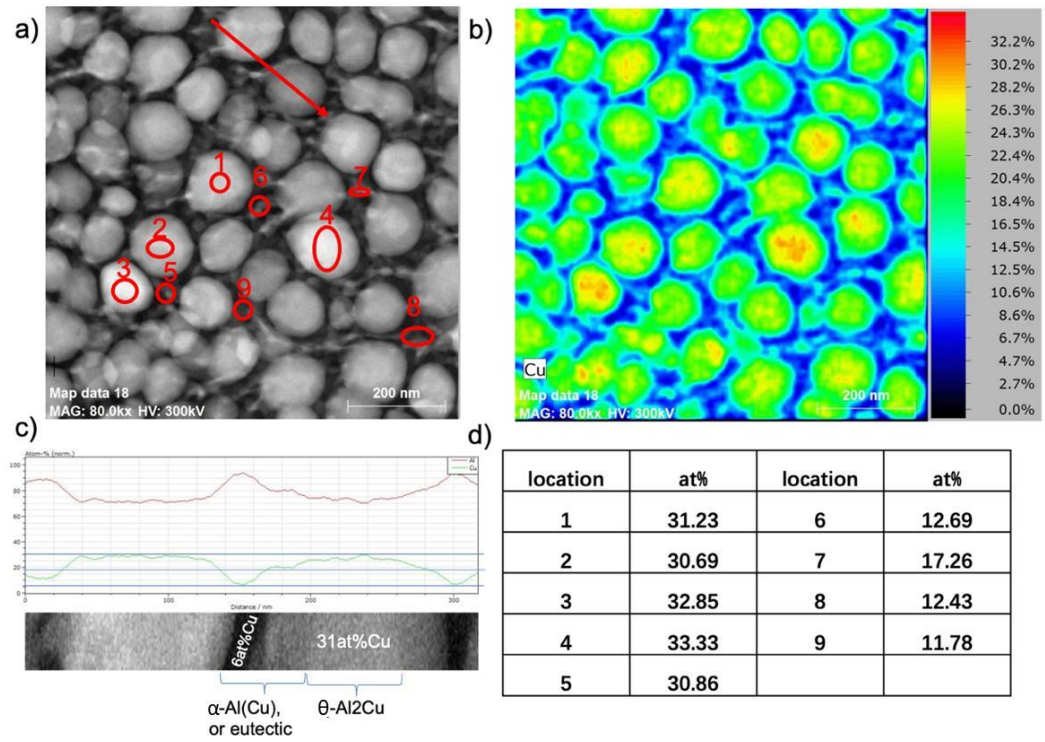

location	at%	location	at%
1	31.23	6	12.69
2	30.69	7	17.26
3	32.85	8	12.43
4	33.33	9	11.78
5	30.86		

Fig. 5: a) HAADF STEM image of the heat-affected zone with the labels of selected areas for Cu composition analysis. b) Associated EDXS-based Cu composition pseudo-color map from 0 at% Cu(dark blue) to 33 at% Cu (red). c) EDXS line scans for Cu and Al composition profiles along line marked by red arrow in a). d) Summary of Cu composition averages for the select regions marked in a).

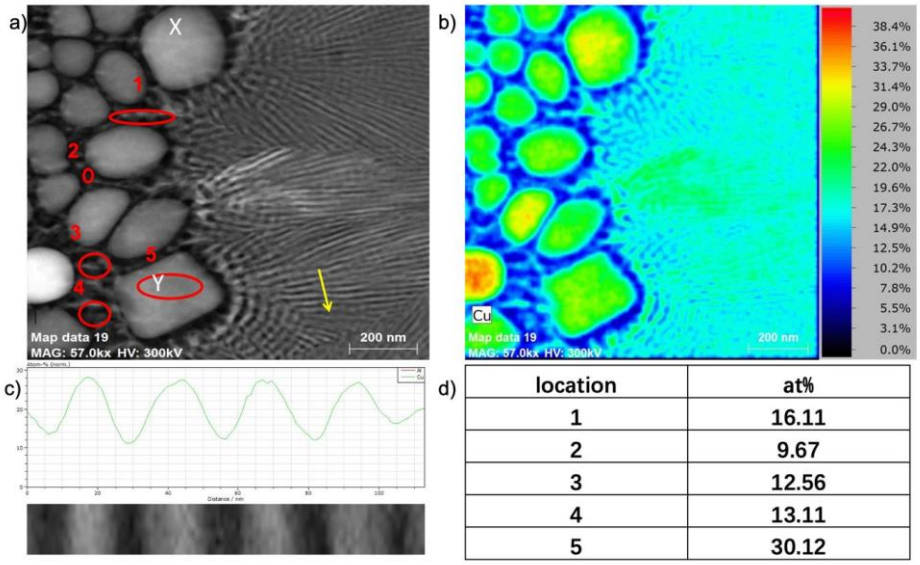

location	at%
1	16.11
2	9.67
3	12.56
4	13.11
5	30.12

Fig. 6: a) STEM HAADF image of the heat-affected zone and eutectic growth zone with labels of select Cu composition analysis region and line scan location across the eutectic pattern, and b) associated EDXS-based Cu composition pseudo-color map of 0at% Cu(dark blue) to 40at% Cu (red). c) Cu composition line profile for lamellar eutectic growth zone marked by the yellow arrow in a). d) Summary of Cu composition averages for the selected region labeled in a).

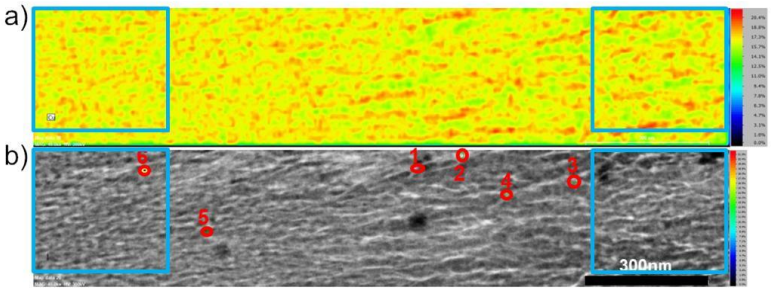

c)

location	at%
1	20.83
2	20.84
3	22.47
4	21.99
5	16.66
6	17.14
7(Field of view)	19.92

Fig. 7: a) EDXS-based Cu composition pseudo-color map for 0 at% Cu(dark blue) to 21 at% Cu (red) and b) STEM HAADF image of the transition/boundary of the eutectic growth zone (Stage I) to α-cell dominated cellular growth zone (Stage II), c) a summary of Cu composition averages for the selected circled regions marked with respective numeral labels in b). The regions delineated in a) and equivalently in b) by rectangles have been used for image analyses to determine the are fractions of the bright and darker contrast imaging phases.

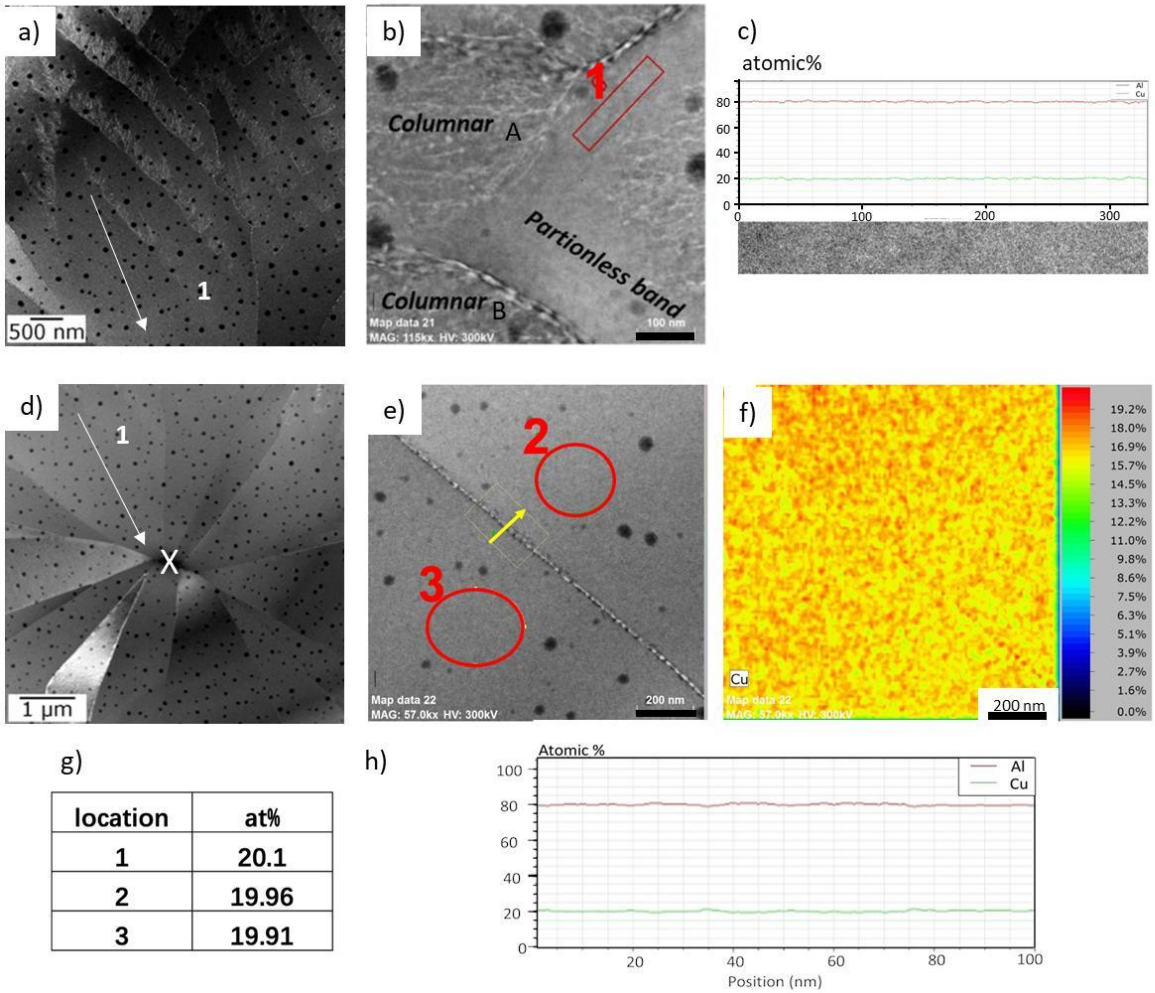

g)

location	at%
1	20.1
2	19.96
3	19.91

h)

Fig. 8: a), b), d) and e) are STEM HAADF images from Zone C of the RS microstructure. The transition of the characteristic banded grain morphology of alternating single-phase and two-phase bands to the central region of Zone C with large single-phase regions is depicted in a) and d). An identical location is marked by the numeral 1 in a) and d). b) depicts the transition from Zone B to Zone C of the RS microstructure. The label Columnar marks neighboring α-Al dominated eutectic cells of Zone B. The upper of the two columnar grains of Zone B exhibits a growth mode change to single-phase growth to form the first single-phase band (label Partionless band) of a banded morphology grain of Zone C. c) EDXS element composition line scans of the region marked by numeral 1 and rectangle in b). d) Terminal single-phase bands formed at the end of RS in the center of Zone C, where label 1 marks the same location as label 1 in a). e) STEM HAADF image of the center of the RS microstructure where the last liquid solidified and two single-phase bands from two different Banded grains in Zone C meet. f) Cu composition map, range of 0 at% Cu (dark blue) to 21 at.% Cu (red) for area imaged in e). g) Examples of average Cu concentrations for area marked 1 in b) and areas marked 2 and 3 in e). h) Average of EDXS elemental composition line scans across the boundary between the two banded grains along the direction indicated by yellow arrow for the area marked in e).

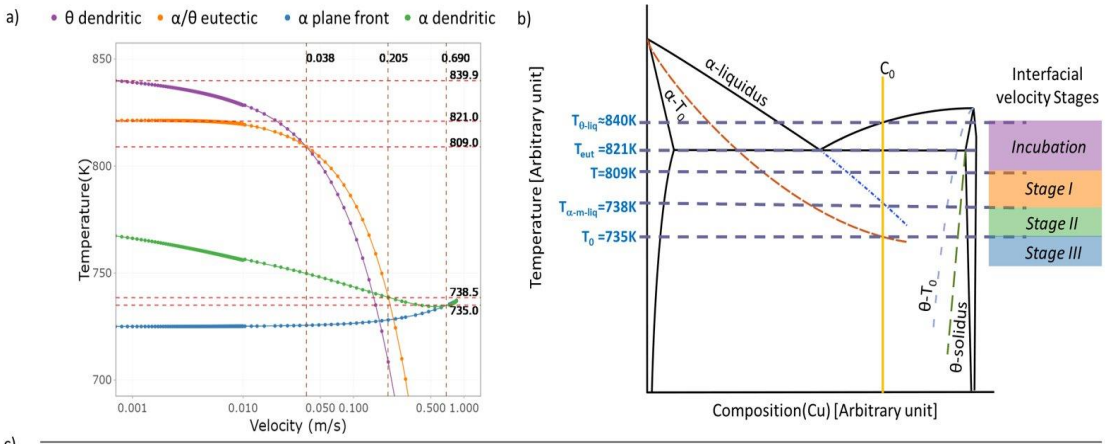

c)

Morphological zones	Growth Mode	Interfacial velocity Stages	Interfacial velocity ranges
HAZ	θ-dendrite	*Incubation*	$V_i < 0.1$m/s
Zone A	θ/α-eutectic, 2 λ & optical lamellar	*Stage I*	0.11m/s < $V_i \leq$ 0.28m/s
Zone B	α dominated eutectic, irregular θ to discontinuous & metastable θ′ (α cell)	*Stage II*	0.3m/s < $V_i \leq$ 0.68m/s
Zone C	Banded & α Plane front, $v>v_a$	*Stage III*	0.7m/s < $V_i = V_a$

Fig. 8: a) Comparison of interface temperature versus interface velocity calculation results for q-phase dendritic, a-phase dendritic, q-a eutectic and a-phase plane front growth in hypereutectic Al-20Cu alloy. b) Schematic of the Al-Cu phase diagram section from α-Al to θ-Al_2Cu. The alloy composition is shown as a solid yellow line and the α-Al liquidus line is shown as a blue dash-dot line. The T_0 lines of α-Al and θ-Al_2Cu are shown as dash lines (light gray – θ, orange - α). The θ-Al_2Cu solidus line is shown as green dash line. At the left side is a schematic illustration of the temperature range of the four distinct microstructure evolution stages as marked at the right side as Incubation, Stage I, Stage II, and Stage III and defined in Fig. 3. c) Summary table of the morphologically distinct microstructure zones, the growth modes, solidification interface velocity evolution stages (see Fig. 3) and ranges of interfacial velocity.

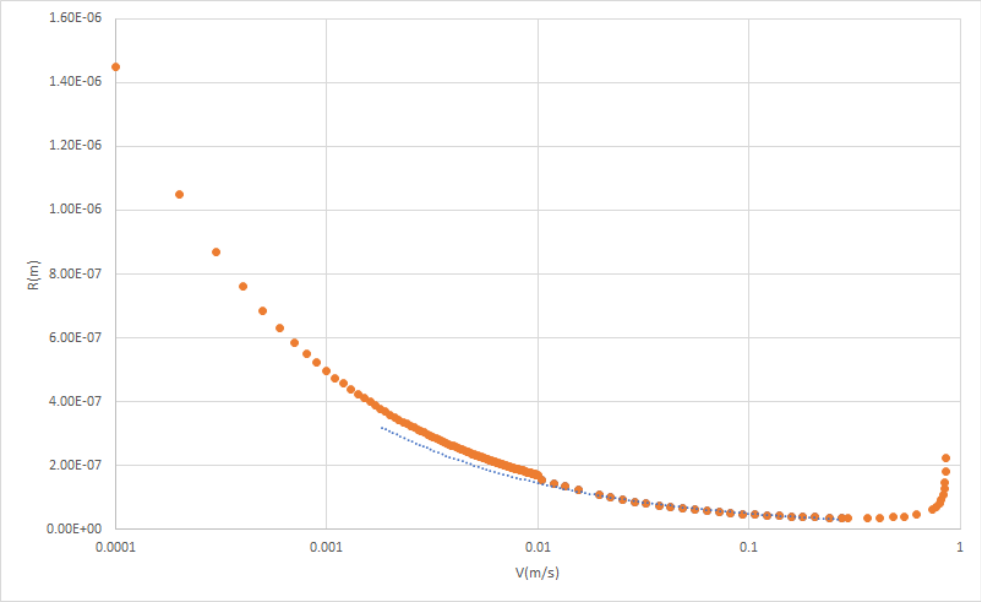

Figure A9: dendritic tip radius prediction at different solidification velocities.

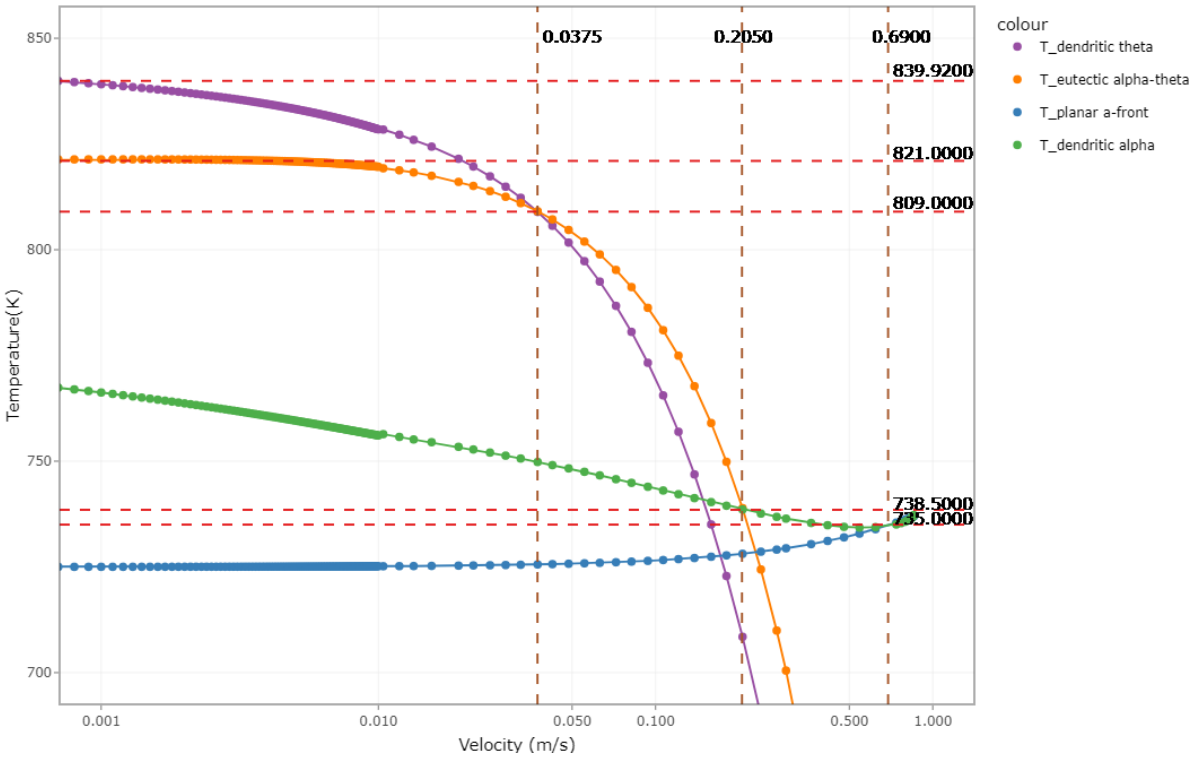

Figure A2: Calculated curves of interface temperature as a function of interface velocity for theta dendritic, alpha dendritic, theta-alpha eutectic and alpha plane front growth for the Al-20at%(37wt%)Cu alloy.

Table

Table 1: Physical parameters of Al-20at%Cu alloy used in calculating the solid-liquid interface temperature.

Parameters	values	unit	Reference
Melting temperature of Al, T_m	933.15	K	[52]
Slope of the liquidus, m_l	4.394		[52]
Diffusivity of Cu in liquid Al, D	3.45e-9	m^2/s	[53]
Solute partitioning coefficient, K_e	1.4		[54]
Interface kinetics coefficient, μ_k	2.3e-3	$ms^{-1}k^{-1}$	[47]
Gibbs-Thomson coefficient of θ, Γ_θ	5.5e-8	Km	[47]
Gas constant, R_g	8.314	J/mol*k	
Velocity of sound in Al, V_0	2e3	m/s	[49]
Eutectic temperature, T_E	821	K	[52]
Gibbs-Thomson coefficient of α, Γ_α	2.4e-7	Km	[49]
Slope of the liquidus for α dendritic, m_{l_α}	-7.85		
Solute partitioning coefficient for α dendritic growth, near 20at%Cu, $K_{e\text{-}\alpha}$	0.638		